Multi-peak Retracking of CryoSat-2 SARIn Waveforms Over Arctic Sea Ice

Di Bella, Alessandro; Kwok, Ronald; Armitage, Thomas W. K.; Skourup, Henriette; Forsberg, René

Published in:
I E E E Transactions on Geoscience and Remote Sensing

Link to article, DOI:
10.1109/TGRS.2020.3022522

Publication date:
2021

Document Version
Publisher's PDF, also known as Version of record

Citation (APA):
Di Bella, A., Kwok, R., Armitage, T. W. K., Skourup, H., & Forsberg, R. (2021). Multi-peak Retracking of CryoSat-2 SARIn Waveforms Over Arctic Sea Ice. *I E E E Transactions on Geoscience and Remote Sensing*, *59*(5), 3776-3792. https://doi.org/10.1109/TGRS.2020.3022522

Multi-peak Retracking of CryoSat-2 SARIn Waveforms Over Arctic Sea Ice

Alessandro Di Bella, Ronald Kwok, *Life Fellow, IEEE*, Thomas W. K. Armitage,
Henriette Skourup, *Member, IEEE*, and René Forsberg

***Abstract*— CryoSat-2 (CS2) is the first mission equipped with a pulse-limited radar altimeter capable of operating in Synthetic Aperture Radar (SAR) Interferometric (SARIn) mode. Over ice sheets and ice caps, CS2 SARIn data have been used to retrieve surface elevations over an across-track ground "swath." This work demonstrates that retracking multiple coherent peaks of CS2 SARIn waveforms, in combination with the interferometric phase, enables to obtain more than one valid height estimate from single SARIn waveforms over Arctic sea ice. For some SARIn waveforms, the scattering from sea ice at the satellite nadir is successfully separated from returns originating from off-nadir leads. An average bias of −1.8 cm is found for absolute sea ice elevations when using a 50% threshold retracker. It is shown that including multiple SARIn peaks and the associated phase difference in the processing does not introduce any bias on the average sea ice freeboard heights compared with the estimates from regular SAR processing schemes, while significantly increasing the number of valid sea surface height retrievals (+55%) and the number of freeboard estimates in the coastal domain and in multi-year ice regions (∼3 times). This results in an average ∼34% reduction of the gridded random freeboard uncertainty, corresponding to a ∼20% reduction of the gridded total sea ice thickness uncertainty. The results of this work show that SARIn acquisitions over Arctic sea ice provide improved spatial coverage and denser sampling of sea level and sea ice freeboard compared with the SAR mode, with accuracy being largely driven by the retracking algorithm.**

***Index Terms*— CryoSat-2 (CS2), interferometry, radar altimetry, retracking, sea ice, swath processing.**

I. INTRODUCTION

Sea ice plays a fundamental role in the global climate system, influencing the planetary albedo [1]—the fraction of incoming solar radiation reflected back into space—and regulating the fluxes of heat, moisture, and momentum between the atmosphere and the ocean [2]. Formation and melting of sea ice alter the ocean salinity at high latitudes, influencing ocean circulation patterns [3]. Besides the scientific interest as a climate indicator, knowledge of the sea ice cover and thickness are important for the shipping and fishery industries, as well as for exploration and off-shore activities [4].

In order to understand our changing climate and safely navigate the Arctic Ocean, extensive and continuous monitoring of the Arctic sea ice is necessary. For the last 25+ years, satellite altimetry has been used to estimate sea ice thickness by measuring directly the sea ice freeboard—the height of the sea ice above the local sea level—and converting it to thickness under the assumption of hydrostatic equilibrium [5]–[10]. Since the measured freeboard and the associated errors are typically multiplied by a factor of ∼9.6 in the freeboard-to-thickness conversion [11], sea ice remote sensing techniques should aim at both improving the accuracy and minimizing the uncertainty of freeboard estimates. The second-largest source of freeboard uncertainty, after the contribution due to the lack of knowledge of the Arctic snow cover [12], originates from the poor knowledge of the sea surface height (SSH) in ice-covered regions [13]. Here, the SSH is directly measured from leads—fractures in the sea ice cover caused by divergent ice motion—and its uncertainty is, therefore, determined by the number and spatial distribution of leads.

The European Space Agency's (ESA) CryoSat-2 (CS2) mission is the first satellite radar altimetry mission flying a Ku-band pulse-width limited radar altimeter equipped with two antennas for single-pass interferometric capability. In the Arctic Ocean, the SAR Interferometric Radar ALtimeter (SIRAL) operates in two scientific measurement modes: the Synthetic Aperture Radar (SAR) mode and the SAR-Interferometric (SARIn) mode. In both modes, the along-track resolution of the instrument is improved using the coherence of the emitted pulses to perform Delay/Doppler processing [14]. When operating in SARIn mode, SAR processing is combined with across-track interferometry exploiting the echoes received by the second antenna, which allows to determine the across-track location where the echo originated. The work in [15] demonstrated that the CS2 SARIn mode enables to process "snagged" waveforms, i.e., waveforms whose power echo is dominated by the strong reflection from off-nadir leads [16]. Common SAR altimetry processing schemes, not using the phase information, attempt to discard such waveforms that, otherwise, cause an overestimation of the range. The phase information available in the CS2 SARIn mode can be used to correct for said range error and retrieve a larger number of valid SSH measurements, which, ultimately, increases the accuracy and reduces the uncertainty of the area-averaged SSH [15]. Building on their work, Di Bella *et al.* [17] found a 29% average reduction

---

Manuscript received April 29, 2020; revised July 30, 2020; accepted August 31, 2020. Date of publication September 25, 2020; date of current version April 22, 2021. *(Corresponding author: Alessandro Di Bella.)*

Alessandro Di Bella, Henriette Skourup, and René Forsberg are with DTU Space, National Space Institute, Technical University of Denmark, 2800 Kongens Lyngby, Denmark (e-mail: adia@space.dtu.dk; hsk@space.dtu.dk; rf@space.dtu.dk).

Ronald Kwok is with Polar Science Center, Applied Physics Laboratory, University of Washington, Seattle, WA 98105 USA (e-mail: rkwok01@uw.edu).

Thomas W. K. Armitage was with Jet Propulsion Laboratory, California Institute of Technology, Pasadena, CA 91109 USA (e-mail: tom.w.armitage@gmail.com).

Color versions of one or more of the figures in this article are available online at https://ieeexplore.ieee.org.

Digital Object Identifier 10.1109/TGRS.2020.3022522

of the point random freeboard uncertainty along a single CS2 track, when including the SARIn phase information in the processing. The same work observed no bias between the freeboard heights retrieved using SARIn data with or without the associated phase information.

Despite this finding, no publicly available product to date includes the SARIn phase information in the estimation of sea ice freeboard and thickness. While the main reason is likely to be the scarce SARIn coverage of the Arctic Ocean, currently limited to coastal areas, a more detailed assessment of how the CS2 phase information could benefit sea ice freeboard and thickness retrievals would not only be interesting for the sea ice and polar oceanography communities, but it would contribute to the discussion and the design of future polar satellite altimetry missions.

This work investigates the potential and limitations of the CS2 SARIn acquisition mode for sea ice applications. Swath processing of CS2 SARIn waveforms [18] is able to provide multiple across-track surface elevations in regions with a complex topography, such as ice sheets and ice caps [19], [20]. Despite the relative flatness characterizing the Arctic Ocean and sea ice-covered regions, this work aims to assess if retracking multiple coherent peaks of CS2 SARIn waveforms over Arctic sea ice can produce more than one valid height estimate from single SARIn waveforms. This is done by proposing and implementing, for the first time over sea ice, a multi-peak retracker that additionally includes a side lobes filter algorithm to enhance the selection of relevant waveform peaks. The implications for the accuracy and uncertainty of both Arctic sea ice freeboard and thickness estimates are also investigated.

The next section provides the details about the CS2 and the auxiliary data used in this study, and Section III describes the methodology and data processing applied to CS2 data. The main results are presented and discussed in Sections IV and V, respectively, and a summary of this work is provided in Section VI.

II. DATA

A. ESA CS2

In the Arctic region, CS2 operates mainly in SAR mode, with the exception of coastal areas where data are acquired in SARIn mode. Until October 2014, the SARIn mode was extended to the Wingham Box—a small region in the Arctic between 80–85°N and 100–140°W—to test SARIn capabilities. This work focuses on the processing of 20-Hz level 1b (L1b) SARIn waveforms acquired in the Arctic Ocean mainly between January and April 2014 (baseline C version of the data). In order to compute sea ice freeboard estimates over the entire Arctic basin, SAR waveforms are also processed and included in the analysis. The ground resolution of the SIRAL instrument operating in both SAR and SARIn acquisition modes extends for ∼450 and ∼1650 m in the along- and across-track directions, respectively [21]. Due to an issue with the SARIn phase difference at the boundaries of the SARIn acquisition mask affecting the CS2 Baseline C product [22], this study utilizes a reprocessed version of the data set with improved accuracy of the phase difference. In addition, the CS2 mispointing angles available in the official ESA Baseline C product are replaced with an updated version [23], which has also been included in the new CS2 Baseline D data product [24].

B. NASA Operation IceBridge

This study uses airborne data from the NASA's Operation IceBridge (OIB) campaigns collected between March 12 and 31, 2014. The difference between the laser freeboard—the height of the air/snow interface above the local sea level measured by the laser scanner—and the snow depth—measured by the ultra-wideband snow radar—is compared in this work to satellite-derived freeboard heights. The following analysis utilizes the OIB L4 Sea Ice Freeboard, Snow Depth, and Thickness Quick Look product, as the fully consolidated product [25] is not yet available for 2014. The Quick Look data set has a larger uncertainty compared with the consolidated product since it relies on near real-time GPS data, and a simplified algorithm to identify leads in Digital Mapping System (DMS) images[1] compared with the one used for the consolidate products [26]. Nevertheless, the Quick Look data set is found to be suitable for the analysis carried out in this work. All measurements, averaged along track, are provided at a ground resolution of 40 m.

C. NASA USGS Landsat 8

CS2 lead detection capabilities are assessed in this work with data from the Operational Land Imager (OLI) instrument onboard the Landsat 8 (LS8) mission. LS8 is a collaboration between NASA and the United States Geological Survey (USGS), providing moderate-resolution measurements of the Earth's terrestrial and polar regions in the visible, near-infrared, short wave infrared, and thermal infrared. This study utilizes data in the panchromatic band (band 8) available in the level 1 product at a 15-m resolution. Pixel digital numbers are converted to top of the atmosphere reflectance estimates following the procedure outlined in [27], and the values of reflectance in the range 0–1 are stretched between 0.25 and 0.7 to enhance image contrast over sea ice.

D. Sea Ice Concentration and Sea Ice Type

Sea ice concentration and sea ice types are provided by the European Organisation for the Exploitation of Meteorological Satellites (EUMETSAT) OSI Satellite Application Facility (OSI SAF) system. The sea ice concentration product (OSI-401-b) uses a combination of brightness temperatures from microwave radiometry and numerical weather prediction data from the European Centre for Medium-Range Weather Forecasts (ECMWF) [28]. Sea ice type estimates (OSI-403-c) are also based on data from microwave radiometry combined, using a Bayesian multisensor approach, with measurements

---

[1] Documentation available at https://daacdata.apps.nsidc.org/pub/DATASETS/ICEBRIDGE/Evaluation_Products/IceBridge_Sea_Ice_Freeboard_SnowDepth_and_Thickness_QuickLook/Documentation/icebridge_ql_products_2014.pdf

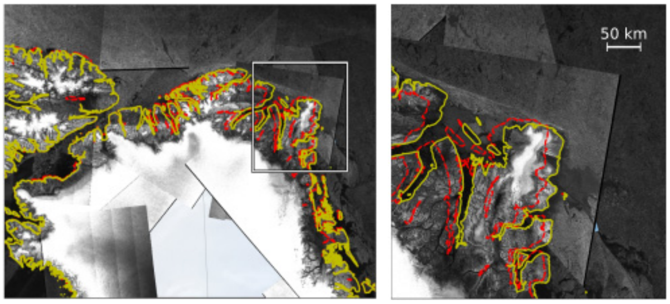

Fig. 1. Comparison between the GSHHG coastline (red), used by the CS2 L1b product for surface classification, and the OpenStreetMapData coastline (yellow). The area inside the white box in the left figure is enlarged to the right, showing the very good agreement of the OpenStreetMapData data set with the Sentinel-1 mosaic in the background, whereas GSHHG data deviate ∼20 km from the actual coastline in this region.

from the Advanced Scatterometer (ASCAT) and ECMWF data for atmospheric corrections. Both products have a daily temporal resolution and are distributed on a 10-km Polar Stereographic grid.

E. High-Resolution Coastline

A high-resolution coastline is necessary to assess CS2 SARIn capabilities in coastal areas and in the proximity of fjords and small islands in the Arctic. The surface classification flag originally available in the CS2 product—based on the Global Self-consistent, Hierarchical, High-resolution Geography database (GSHHG) [29]—is not used in this work as the GSHHG data set is found to deviate up to ∼20 km from the actual coastline in Northeastern Greenland. For this reason, satellite measurements over land are filtered out using a high-resolution land polygons data set from the OpenStreetMapData project (https://osmdata.openstreetmap.de/data/land-polygons.html), which seems to perform better than GSHHG in the areas of interest to this study. A comparison of the two coastlines in Northern Greenland is available in Fig. 1.

III. METHODOLOGY AND DATA PROCESSING

The majority of the currently available sea ice thickness estimates from satellite radar altimetry are obtained based on the procedure first introduced by [5]: waveforms along satellite tracks are classified as returns originating from either sea ice or leads by looking at their shape and maximum power, both determined mainly by surface roughness. The height of the sensed surface is then computed by the so-called retracking algorithm, which determines the point on the waveform, or on a fitting function, most likely representing the range to the surface. Lead heights are interpolated to estimate the SSH along the satellite track, which is then subtracted from the sea ice elevations to estimate freeboard heights. Finally, taking into account snow and sea ice properties, sea ice freeboard heights are converted to thickness estimates under the assumption of hydrostatic equilibrium.

The following sections describe, in detail, the sea ice thickness processing chain used in this study for CS2 SAR and SARIn L1b waveforms, referred to in this work as the DTU Space multi-peak processor (DTU-MPP). The main processing steps performed for each CS2 orbit are summarized in Fig. 2, with a special focus on SARIn multi-peaked waveforms.

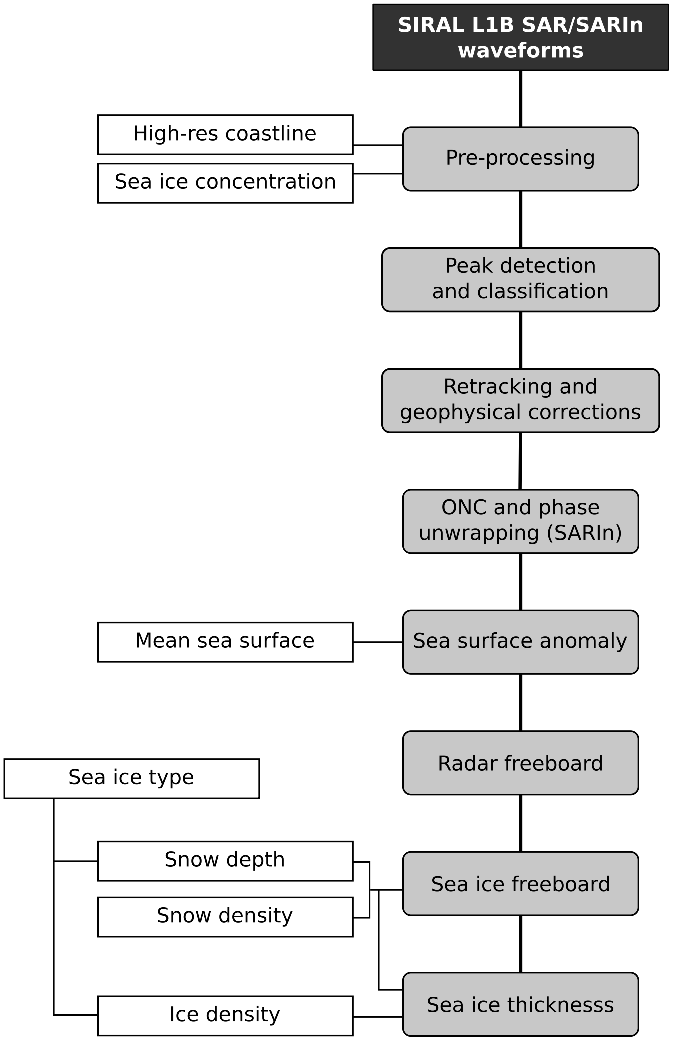

Fig. 2. Diagram summarizing the algorithm used by DTU-MPP to retrieve sea ice freeboard and thickness along each CS2 orbit. White boxes represent external auxiliary data.

A. Preprocessing

Basic waveform filtering is performed according to the L1b product quality flags, as described in [21]. In addition, the power of SARIn waveforms is divided by a factor two to overcome an issue in the Baseline C level 1 Instrument Processing Facility (IPF1)—the software used by ESA to compute the L1b waveforms.[2] Faulty coherence values larger than one, as observed in [30], are set to zero.

Measurements over land are discarded using the OpenStreetMapData high-resolution coastline, and the OSI SAF sea ice concentration product is used to select waveforms located in grid cells having a concentration larger than 70% to ensure that the analyzed grid cells are mostly covered by sea ice [13]. Measurements in the coastal regions north of Greenland and

---

[2] This is only necessary for Baseline C waveforms as the issue has been corrected in the latest Baseline D version of the CS2 product [24]

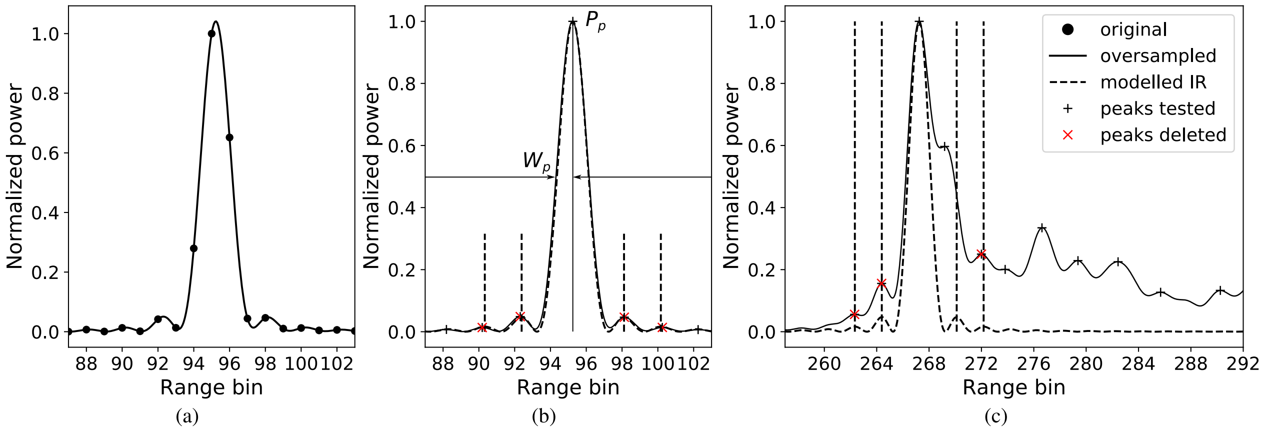

Fig. 3. Example of zero-padding interpolation on (a) specular CS2 waveform (b) sidelobe filtering of a specular and (c) diffuse CS2 oversampled waveform. Peaks corresponding to the two strongest side lobes of the SIRAL impulse response (IR) are discarded. The power is normalized with respect to the waveform maximum power. The peak power P_p and the half-width at the half-power point W_p used for the classification of the first peak are shown in (b).

the Canadian archipelago, where no valid sea ice concentration is reported in the OSI SAF product, are also retained to explore the coastal capabilities of CS2 SARIn acquisition mode—these areas have a sea ice concentration well above 70% for the time frame used in this study, i.e., from January to April.

Additional waveform filtering is performed using thresholds for the signal-to-noise ratio (SNR) and the Pulse Peakiness (PP) of the waveforms, so as to exclude waveforms too noisy to allow for the identification of a clear leading edge and remaining echoes likely originating from the ocean [17]. The waveform SNR is defined as

$$\mathrm{SNR} = 10\log_{10}\left(\frac{P_{\max}}{P_N}\right) \tag{1}$$

where $P_{\max}$ is the maximum power and P_N is the thermal noise of the waveform. P_N is defined as the average power of the waveform computed using the first J range bins, with $J = 20$ and $J = 80$ for SAR and SARIn waveforms, respectively. The different values of J are due to the four times larger range window of SARIn waveforms compared with SAR waveforms. The PP parameter used in this study is defined in [15] as

$$\mathrm{PP} = \frac{P_{\max}}{\sum_{i=1}^{N_B} P_i} \tag{2}$$

where N_B is the total number of range bins of the waveform. Only waveforms with SNR $>$ 15 dB and PP > 0.012 are selected, based on the work in [17] and [13]. SAR waveforms with $0.1 < \mathrm{PP} < 0.25$ are additionally discarded as they are assumed to be affected by snagging, which cannot be corrected for in the SAR mode, and would affect significantly the elevations retrieved from these waveforms [15], [17]. While this step does reduce the number of snagged waveforms that are processed, it also reduces the number of leads detected. Waveform discrimination in the ice-covered oceans is still a challenging procedure and is reflected in the many techniques that have been proposed throughout the years [31].

B. Peak Detection and Classification

CS2 waveforms are oversampled in the frequency domain by applying an order 16 zero-padding, so as to refine the position of the peaks [8], as this is not accurately described by the original waveform samples [see Fig. 3(a)]. Besides refining the position of the peaks, the oversampling procedure reveals side lobes originating from the impulse response (IR) of the SIRAL instrument. This effect is especially visible in strong and specular returns originating from leads, where the echo received back to the satellite looks very much like the transmitted compressed pulse s, described as a function of the range r in [32] as

$$s(r) = \mathrm{sinc}^2\left(\frac{2\pi B_w r}{c}\right). \tag{3}$$

Here, $B_w = 320$ MHz is the radar bandwidth, c is the speed of light, and $\mathrm{sinc}(x) = \sin(x)/x$. The width of the main lobe at the half-power point of the SIRAL compressed pulse defines the instrument range resolution as ~46.84 cm [33].

Before peak detection, the instrument IR (dashed line in Fig. 3) is computed in the range bin space for each waveform, and the peaks located in correspondence of the first two strongest side lobes (red crosses in Fig. 3) are discarded. The algorithm allows for a maximum deviation of $\pm 1/2$ of a range bin from the location of the modeled side lobes (the vertical dashed lines in Fig. 3), to account for the fact that the received waveform is not the perfect copy of the modeled instrument IR, due to the measurement noise and the interaction of the transmitted signal with the ground. This procedure is performed for strong and specular reflections from leads as well as for more diffusive power echoes since also some of the CS2 waveforms originating from sea ice show similar contributions from SIRAL side lobes [see Fig. 3(c)]. This technique is found to be especially effective in detecting peaks in front of the waveforms leading edge that are not associated with real surface returns, whereas an approach based on a power threshold alone might either not detect some of these side lobes or discard peaks corresponding to actual returns from the surface.

The remaining significant peaks are separated by the algorithm into first and subsequent peaks. Over relatively flat surfaces, such as the Arctic Ocean, the first peak of a waveform usually corresponds to the main reflection originating on the ground from the point of closest approach (POCA) at a location close to the satellite nadir. In this study, the first significant peak of a waveform is selected as the first peak having a power above 30% of the maximum waveform power (and always above an absolute noise threshold of 5 fW), so as to suppress any potential noisy peaks left on the waveform leading edge after side lobes filtering. While only the first significant peak is selected in SAR waveforms, this study investigates the origin of subsequent peaks of SARIn echoes. Peaks on the waveform trailing edge, i.e., located to the right of the peak associated with the main ground reflection, result from scattering occurring at both sides, and increasingly further away, from the POCA [34]. A measure of the extent to which the received power originates from one of the two sides of the POCA, rather than a mixture of the two, is provided by the cross-channel coherence [35], ranging from zero to one, included in the CS2 L1b product. Echoes from dominant features on the ground, e.g., leads, are characterized by a high value of coherence, indicating that the power received comes predominantly from one distinct location in the footprint that can be determined using the interferometric phase measurement [15]. In this work, only subsequent peaks of SARIn waveforms having a coherence larger than 0.9 are selected.

The first peak classification is carried out using a combination of the peak power P_p and the half-width of the peak at the half-power point W_p [see Fig. 3(b)]. The analysis of these two parameters from first unambiguous waveform peaks in the Arctic Ocean [36] shows that they can be successfully used to detect open water in ice-covered regions. In this work, the first peaks of both SAR and SARIn waveforms are classified as reflections coming from

$$\begin{cases} \text{lead}, & \text{if } (P_p > 35) \wedge (W_p < W_l(P_p)) \\ \text{sea ice}, & \text{otherwise} \end{cases} \tag{4}$$

with P_p expressed in dB-fW. The value of W_l depends on the peak power according to

$$W_l = \begin{cases} 28, & \text{if } P_p \leq 35 \\ 28 - 0.184(P_p - 35), & \text{if } 35 < P_p < 60 \\ 23.4, & \text{if } P_p \geq 60 \end{cases} \tag{5}$$

with W_p and W_l both expressed in cm. In (5), the value of $W_l = 23.4$ cm corresponds to the half-width at the half-power point of the SIRAL IR, which is expected for very strong specular returns with $P_p \geq 60$ dB-fW. The values of $W_l = 28$ cm and $P_p = 35$ dB-fW are based on [36] and adapted using coincident Sentinel-1 SAR images to aid classification. Values of W_l for $35 < P_p < 60$ dB-fW are determined assuming a linear relationship between the half-width of the peak and the peak power in dB-fW [36].

Peaks occurring after the first selected peak are assumed in this work to originate from distinct off-nadir specular features on the ground. The classification in (4) and (5), however, cannot be applied directly to SARIn subsequent peaks since both the attenuation from the antenna beam pattern and a portion of the energy being scattered away from the instrument make off-nadir returns from leads not as powerful as those originating at the satellite nadir. Suitable subsequent peaks of SARIn waveforms are selected instead following an approach based on their final retracked elevation and explained, in more detail, in Section III-E.

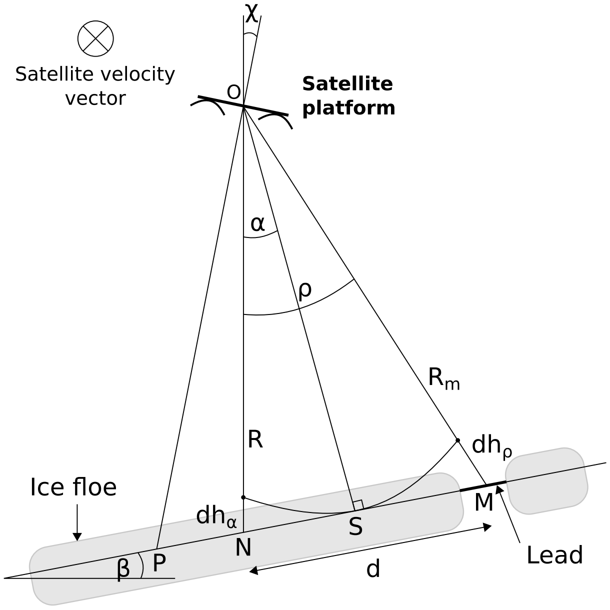

Fig. 4. Geometry for the ONC assuming the satellite velocity vector entering the page. OP is the antenna boresight direction, and χ is the satellite platform roll angle measured from the satellite nadir (N). ρ is the angle between the nadir and the lead (M), and R and R_m are the ranges to the nadir and to the lead, respectively, while d is the across-track distance to the lead (NM). β is the across-track surface slope, and α is the angle between the nadir and the POCA (S). dh_ρ and dh_α are the range errors due to off-nadir ranging and the across-track slope, respectively, and the total range correction is $\text{ONC} = dh_\rho - dh_\alpha$.

C. Retracking

In this work, all peaks are retracked using a 50% threshold retracker, except for subsequent peaks of SARIn waveforms. Since many subsequent peaks do not have an unambiguous half-power point on their rising edge [see Fig. 3(c)], they are instead retracked at the range bin where the peak power occurs. Elevations from subsequent peaks are then corrected to avoid range biases introduced by the choice of a different retracking point. The correction applied equals the half-width at the half-power point of a Gaussian fit around the peak, computed using the first eight oversampled values to the left and to the right of the peak location—which corresponds to using ±1/2 bin in the original range bin space.

All retracked elevations are corrected for atmospheric and tidal effects using the corrections included in the L1b product, as described in [21].

D. Off-Nadir Correction (ONC) and Phase Unwrapping

For SARIn echoes, the interferometric phase available in the L1b product is used to compute the across-track angle of arrival to the location on ground associated with all the selected waveform peaks. A sketch of the geometry associated with off-nadir returns is provided in Fig. 4, which shows the case of a single off-nadir return from a lead. According to [15], the across-track angle of arrival ρ can be estimated as

$$\rho \simeq \frac{\phi}{k_0 B} - \chi \tag{6}$$

where ϕ is the phase difference interpolated at the retracking point of the specific peak, k_0 is the carrier wavenumber, B is the interferometric baseline, and χ is the platform roll bias. For small values of across-track surface slope β, the across-track distance of the return d from the nadir can be approximated by

$$d \simeq R_m \sin(\rho) \simeq R_m \rho \tag{7}$$

where R_m is the measured range to the lead. The total off-nadir correction (ONC) accounts for the range error associated with off-nadir scattering and for the range error caused by the across-track surface slope (dh_ρ and dh_α, respectively, in Fig. 4), and is defined in [15] as

$$\mathrm{ONC} \simeq \frac{\eta R_m}{2}(\rho^2 - 2\rho\alpha) \tag{8}$$

where η is a geometric factor used to correct for the curvature of the Earth [32], and the across-track slope β is converted to an across-track angle to the POCA through $\alpha = \beta/\eta$ [15]. In this work, the ONC is applied to height estimates from all the relevant peaks of SARIn waveforms, independent of their classification and location on the waveform.

The phase difference provided in the CS2 SARIn L1b product is wrapped in the interval $(-\pi, +\pi]$. If part of the waveform originates from scattering occurring outside of the CS2 beam-limited footprint, i.e., further than ~7 km away from the satellite nadir, the phase difference will be discontinuous, showing sudden jumps between the interval extremes. Wrapped values of the phase difference can change the sign of ρ and d in (6) and (7), respectively, displacing the real scattering location to the opposite side of the satellite track. In addition, they cause inaccurate values of ρ that lead to inaccurate estimates of the ONC. Using some basic assumptions, the 1-D phase unwrapping of the CS2 SARIn differential phase can be heavily simplified. In relatively flat areas such as the Arctic Ocean, it is safe to assume that the first significant peak of the waveform either corresponds to the POCA or, even in the case of snagged waveforms, it originates inside the beam-limited footprint. Thus, assuming that the phase difference at the retracking point of the first detected peak is not wrapped and that the phase difference between two consecutive range bins is not aliased, this absolute difference should not be larger than π [37]. Under these conditions, phase unwrapping is performed in this work by detecting jumps in the phase difference after the retracking range bin of the first peak and by either adding or subtracting 2π to the phase value, depending on the sign of the difference between the phase at the two consecutive range bins where the jump occurs. To account for discontinuities in the phase difference caused by measurement noise, phase jumps are detected with independent iterations using different detection thresholds. During every iteration, new values of ONC are computed and added to the retracked heights of subsequent peaks. If the deviation of the new height estimates from the mean sea surface is lower than prior to the phase unwrapping procedure, the old value of phase difference is replaced with the new value. This test is considered to be reliable, as height errors from wrapped phases cause an underestimation of the retracked heights in the order of several tens of meters. The iterative procedure reduces the possibility of detecting false phase wraps and prevents the unwrapping error from accumulating—as a false wrap detected at any range bin would affect values of phase difference at all consecutive bins. After phase unwrapping is performed on SARIn waveforms, the location of the echoes, relocated across track using the new value of phase difference, is tested once more against the high-resolution coastline to discard reflections possibly originating from land.

E. Sea Surface Estimation

The DTU18 Mean Sea Surface (MSS) [38] is subtracted from all retracked and corrected elevations to remove the major component of the height measurement due to the geoid, as well as higher frequency variations in the SSH [39]. This reduces interpolation errors and improves the accuracy of the local SSH especially in areas with few detected leads. In this work, a reference sea surface anomaly ($\mathrm{SSA_{ref}}$) is obtained through the along-track linear interpolation of the lead elevations from peaks with $P_p > 35$ dB-fW, selecting as tie points only specular returns originating close to the satellite nadir. A 25-km running mean filter is applied to smooth height variations caused by measurement noise [13], and the value of $\mathrm{SSA_{ref}}$ is set to be invalid at locations further than 100 km from the closest lead, as interpolation is assumed not to be accurate enough to describe local changes in the sea surface at such scales.

The final along-track SSA is then estimated using the same approach as for $\mathrm{SSA_{ref}}$ but including all peaks classified as leads (see Section III-B) as well as subsequent peaks with retracked elevations within ±15 cm from $\mathrm{SSA_{ref}}$. The 15-cm threshold is chosen empirically.

F. Freeboard and Thickness Estimation

While laboratory measurements showed that radars operating at Ku-band, such as SIRAL, can penetrate a layer of cold and dry snow [40], the analysis performed by [41] on Arctic sea ice shows a strong relationship between penetration depth at the Ku-band and snow temperature. With temperatures close to freezing, they found that the main scattering surface appeared to be closer to the snow/ice interface than the air/snow interface in only 25% of the radar returns compared with the 80% of the returns at lower temperatures. Despite these findings, and due to the lack of knowledge of snow properties in the Arctic basin and their temporal evolution throughout the year, this work assumes that the main scattering horizon for CS2 returns over sea ice coincides with the snow/ice interface—although it is acknowledged that this might introduce a bias in the final freeboard estimates.

A typical schematic of snow-covered Arctic sea ice is illustrated in Fig. 5. Due to its refractive index being larger than one, a snow layer on top of the sea ice has the effect of slowing down the radar signal [42]. Assuming full penetration

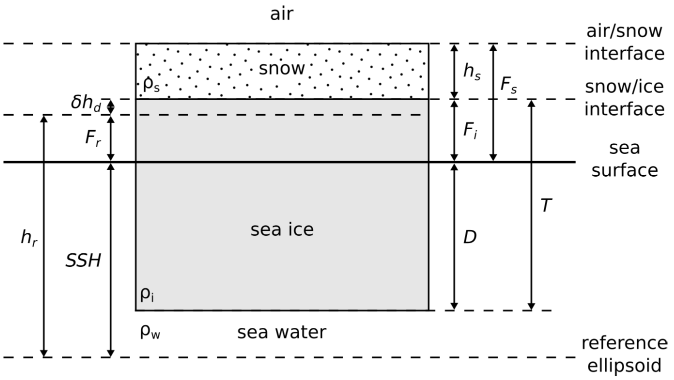

Fig. 5. Schematic drawing showing the radar (F_r), sea ice (F_i), and snow (F_s) freeboard, as well as the sea ice draft (D) and total thickness (T). δh_d is the elevation bias introduced by a layer of snow of depth h_s. h_r is the elevation measured by CS2, while ρ_s, ρ_i, and ρ_w are the density of snow, sea ice, and water, respectively. The drawing is based on the assumption that the main radar scattering horizon coincides with the snow/ice interface.

of the CS2 signal into the snowpack, the sea ice elevations above the MSS h_r measured by CS2 can be then used to compute point estimates of the so-called radar freeboard as $F_r = h_r - \text{SSA}$ and, finally, the sea ice freeboard F_i as

$$F_i = F_r + \delta h_d \tag{9}$$

where δh_d is the bias for the delay due to the lower propagation speed in the snow layer (see Fig. 5) estimated as

$$\delta h_d = h_s \left(\frac{c}{c_s} - 1 \right). \tag{10}$$

Here, h_s is the snow depth and

$$c_s = \frac{c}{\sqrt{1 + 1.7\rho_s + 0.7\rho_s^2}} \tag{11}$$

is the propagation speed in snow, parameterized following [43] as a function of the snow density ρ_s expressed in g/cm^3. Following [8], the snow depth and density used in this study are the time- and space-varying estimates from the modified W99 climatology [44], which accounts for the reduction of the multi-year ice (MYI) fraction observed in the last half-century [45] by halving the original W99 snow depth on first-year ice (FYI) [7], [46]. Sea ice freeboard estimates outside the interval $-\sigma_F < F_i < 2\ \text{m} + \sigma_F$ are discarded, with σ_F being the freeboard uncertainty at a CS2 location (see Section III-G).

For the monthly averages and the large-scale assessments discussed in Section IV, point estimates of freeboard are gridded to the 25-km EASE-Grid 2.0 [47] following the procedure detailed in Appendix A. The methodology used to convert sea ice freeboard to thickness estimates is described in Appendix B.

G. Uncertainties

This study focuses on the random part of the freeboard uncertainty, as this is the quantity that could possibly be reduced by an increase in the amount of processed data. Assuming independent and uncorrelated errors, the uncertainty of a single CS2 radar freeboard estimate σ_{F_r} can be written from [13] as

$$\sigma_{F_r}^2 = \sigma_{L1b}^2 + \sigma_{\text{SSA}}^2 \tag{12}$$

where σ_{L1b} is the total random height uncertainty for a CS2 L1b measurement, estimated as 11.6 and 15.2 cm for SAR and SARIn acquisitions, respectively [11]. The mode-dependent value of uncertainty is due to the larger speckle noise affecting SARIn acquisitions, as this mode uses a lower burst repetition frequency compared with the SAR mode. The uncertainty of the SSA σ_{SSA} generally depends on the amount of lead measurements available along the satellite track. The value of σ_{SSA} is determined in this work by taking the standard deviation of the lead heights within the same 25-km moving window used to estimate the SSA in Section III-E. In the case that no leads are present inside the moving window, σ_{SSA} takes the value of the deviation of the interpolated SSA from the mean CS2 sea ice elevation inside the moving window [13]. Finally, if there is only one lead elevation inside the window, then $\sigma_{\text{SSA}}^2 = \sigma_{L1b}^2$ for SAR acquisitions while $\sigma_{\text{SSA}}^2 = \sigma_{L1b}^2 + \sigma_{\text{ONC}}^2$ for SARIn measurements, where the contribution of the ONC σ_{ONC} is included in the total uncertainty. According to [15], σ_{ONC} can be defined as

$$\sigma_{\text{ONC}}^2 \simeq \eta^2 R_m^2 \left(|\rho - \alpha|^2 \sigma_\rho^2 + \rho^2 \sigma_\alpha^2 \right) \tag{13}$$

where σ_ρ and σ_α are the uncertainties of the angles ρ and α, respectively, in Fig. 4. While the value of σ_ρ is assumed in this work to be 90 μrad, based on the estimations made by [32], σ_α depends on the across-track slope β. In [15], a geoid was removed from the elevations so that the remaining components of σ_α—estimated to be equal to 20 μrad in [48]—would arise from the local dynamic topography, tidal variations in the SSH and from the method used to interpolate the across-track slope of the geoid. By subtracting an MSS from the retracked elevations, σ_α would likely be lower than 20 μrad, as the mean dynamic topography would also be removed. However, precise estimates of uncertainty for the DTU18 MSS used in this work are not available, and 20 μrad is also used in this study as a conservative value for σ_α.

The uncertainty of the sea ice freeboard is by definition larger than the uncertainty of the radar freeboard, as it includes the error contribution from the snow loading. Assuming that the radar penetrates the snow pack completely and that all uncertainties are uncorrelated, the sea ice freeboard uncertainty σ_{F_i} can be written as

$$\sigma_{F_i}^2 = \sigma_{F_r}^2 + \sigma_{\delta h_d}^2 \tag{14}$$

where the uncertainty due to the path-delay correction $\sigma_{\delta h_d}$ can be computed using the Gaussian propagation of the uncertainty on (10) and (11) as

$$\sigma_{\delta h_d}^2 = \left(\frac{\partial \delta h_d}{\partial h_s} \right)^2 \sigma_{h_s}^2 + \left(\frac{\partial \delta h_d}{\partial c_s} \right)^2 \sigma_{c_s}^2 \tag{15}$$

with

$$\sigma_{c_s}^2 = \left(\frac{\partial c_s}{\partial \rho_s} \right)^2 \sigma_{\rho_s}^2. \tag{16}$$

Both the uncertainty of the snow depth σ_{h_s} and the snow density σ_{c_s} provided by the W99 climatology are assumed to be systematic, as they are based on the interannual variability of field measurements reported in [44]. Thus, in the following analysis, the random part of the uncertainty of both radar and sea ice freeboard is considered to be the same—described by (12)—and referred to as σ_F.

Gridded estimates of freeboard uncertainty are obtained according to Appendix A, while the uncertainty of thickness estimates is discussed in Appendix B. It is important to remember that the uncertainties associated with the retracking method and the geophysical corrections are not taken into account by this study, as their contribution would not be reduced by increasing the number of measurements. Furthermore, all the random uncertainty contributions are assumed to be uncorrelated. However, it is acknowledged that the uncertainty estimates presented in this work are an approximation, and that further investigation of the covariance of individual error contributions is needed [13].

IV. Results

A. Multiple Peaks, Lead Detection, and ONC

To investigate the origin of subsequent peaks of SARIn waveforms, a CS2 SARIn track over the Western coast of the Bolshevik Island, in the Kara Sea, is compared with an LS8 image in Fig. 6. Both data from CS2 and LS8 were acquired on March 25, 2016, with CS2 flying over the region 4 h after LS8. No sea ice drift correction is applied to LS8 pixels as the analysis of coincident optical images in the same region (not shown here) shows an average eastwards drift of ~250 m over a full day. The resulting average ~40-m drift occurring in the 4 h separating LS8 and CS2 acquisitions is assumed to be negligible in the following analysis. Blue dots in Fig. 6 represent peaks classified as sea ice by DTU-MPP, while red dots are waveform peaks classified as reflections from leads. All peaks are relocated across track using the CS2 phase information as described in Section III-D. The threshold-based first peak classification algorithm picks up some of the tiny cracks in the sea ice in the upper part of the track. The classification of a part of the refrozen lead as sea ice is due to peak power values just below the threshold used for lead detection (see Section III-B), possibly caused by slightly rougher ice in the left part of the lead than in the right part—which, in the image, appears slightly whiter.

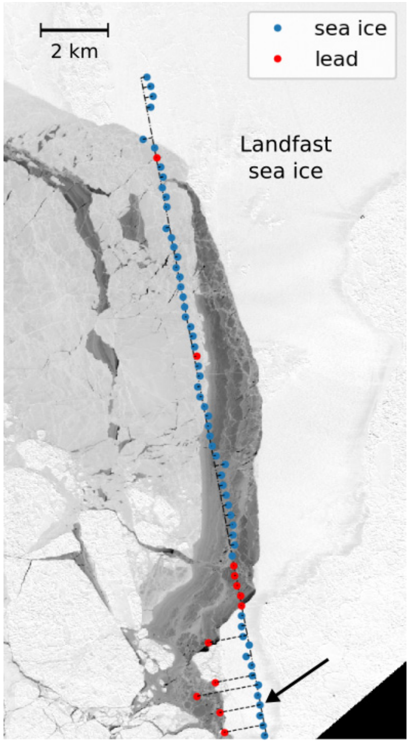

Fig. 6. CS2 SARIn track over the Western coast of the Bolshevik Island superposed on an LS8 optical image. Both data were acquired on March 25, 2016. The lower part of the track shows some off-nadir returns from the refrozen lead successfully separated from nadir returns originating from sea ice. Black arrow indicates the location of the waveform shown in Fig. 7.

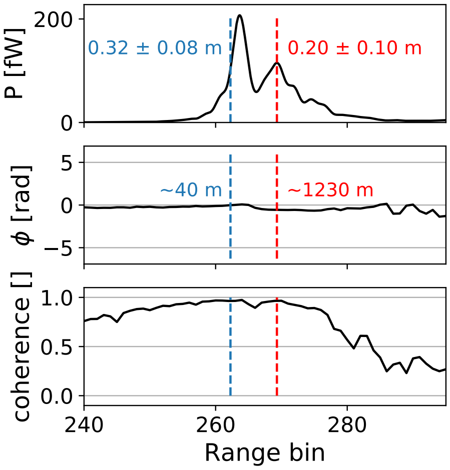

Fig. 7. Power (P), phase difference (ϕ), and coherence measured by CS2 for the waveform highlighted by the black arrow in Fig. 6. Blue and red vertical dashed lines represent the retracking point of the sea ice and the lead peak, respectively. The retracked elevations above the DTU18 MSS are reported in the top figure for both peaks, and the lead elevation includes the correction to account for the different retracking point chosen by the retracker for first and subsequent peaks (see Section III-C). The middle figure shows the estimated across-track distance of the returns from the satellite nadir. The effect of the platform roll angle is removed from the phase difference so that $\phi = 0$ indicates returns from the satellite nadir.

The most interesting features appear in the lower part of the track in Fig. 6 where, for some CS2 SARIn waveforms, it is possible to separate the contribution of sea ice scattering originating close to the satellite nadir from the off-nadir lead returns. The power, phase difference, and coherence of the waveform corresponding to the black arrow in Fig. 6 are shown in the top, middle, and bottom figures, respectively, of Fig. 7. The vertical lines identify the retracking point of the sea ice peak, in blue, and the lead peak, in red. The phase difference at the retracking points is used to compute the across-track distance and the ONC for the respective waveform peak (see Section III-D). The combination of the phase information with coherence values close to one suggests the first peak to originate close to the satellite nadir and the second peak to originate from a single region on the ground located at ~1.2-km off-nadir. The retracked elevations for the sea ice and lead peak are estimated to be 0.32 ± 0.08 and 0.20 ± 0.10 m

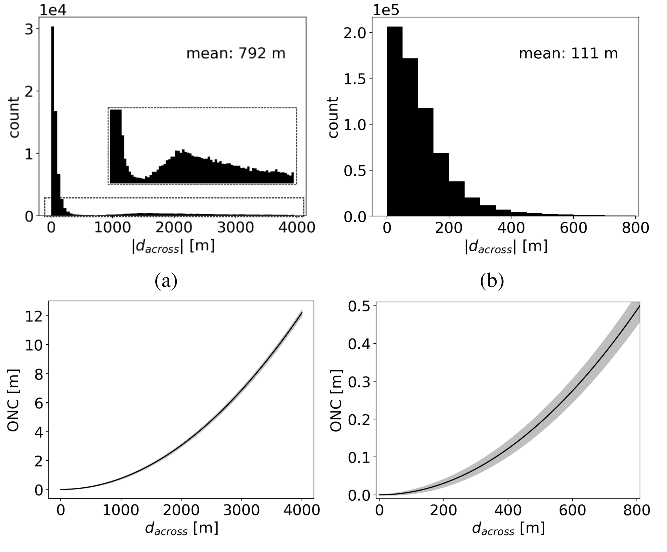

(a) (b)

(c) (d)

Fig. 8. Absolute across-track distance distribution of (a) lead and (b) sea ice peaks obtained with a 50-m binning. The rectangle at the bottom of (a) is enlarged in the floating panel. Theoretical values of ONC from (7) and (8) are plotted for across-track distances up to (c) 4000 and (d) 800 m, assuming an average CS2 altitude of 730 km, and both satellite platform roll angle χ and surface slope β equal to zero. Shaded areas represent the ONC uncertainty according to (13).

TABLE I

PERCENTAGE OF CS2 SARIN WAVEFORMS SHOWING USABLE MULTIPLE PEAKS IN 2014

	Jan	**Feb**	**Mar**	**Apr**
FYI	2.4	2.2	2.1	2.6
MYI	2.2	2.2	1.9	1.9
All	**2.3**	**2.2**	**2.0**	**2.2**

above the DTU18 MSS, respectively. The height estimate from the second peak includes the additional correction to account for the different retracker used for sea ice and lead peaks. The height uncertainty is computed as $(\sigma_{L1b}^2 + \sigma_{\text{ONC}}^2)^{1/2}$ and shows how parts of the echo originating off-nadir are affected by a larger uncertainty [also visible in Fig. 8(c) and (d)]. The resulting 12-cm freeboard height—computed from a single CS2 waveform—is a reasonable estimate for a region with predominantly FYI (see Fig. 10). This example, representative of all the double-peaked waveforms in the lower part of the CS2 track in Fig. 6, suggests that by retracking multiple peaks of some CS2 SARIn waveforms over sea ice, it is possible to obtain more than one valid height estimate from a single waveform.

In the rest of the Arctic Ocean where CS2 operates in SARIn mode—the region within the dashed red boundaries in Fig. 9(a)—the number of multi-peaked waveforms included in the processing is on average $\sim$2% of the available waveforms for each month in the period from January to April 2014 (see Table I). The similar spatial distribution of multi-peaked waveforms in FYI and MYI regions shows that off-nadir scattering occurs, and is detected by CS2, over different kinds

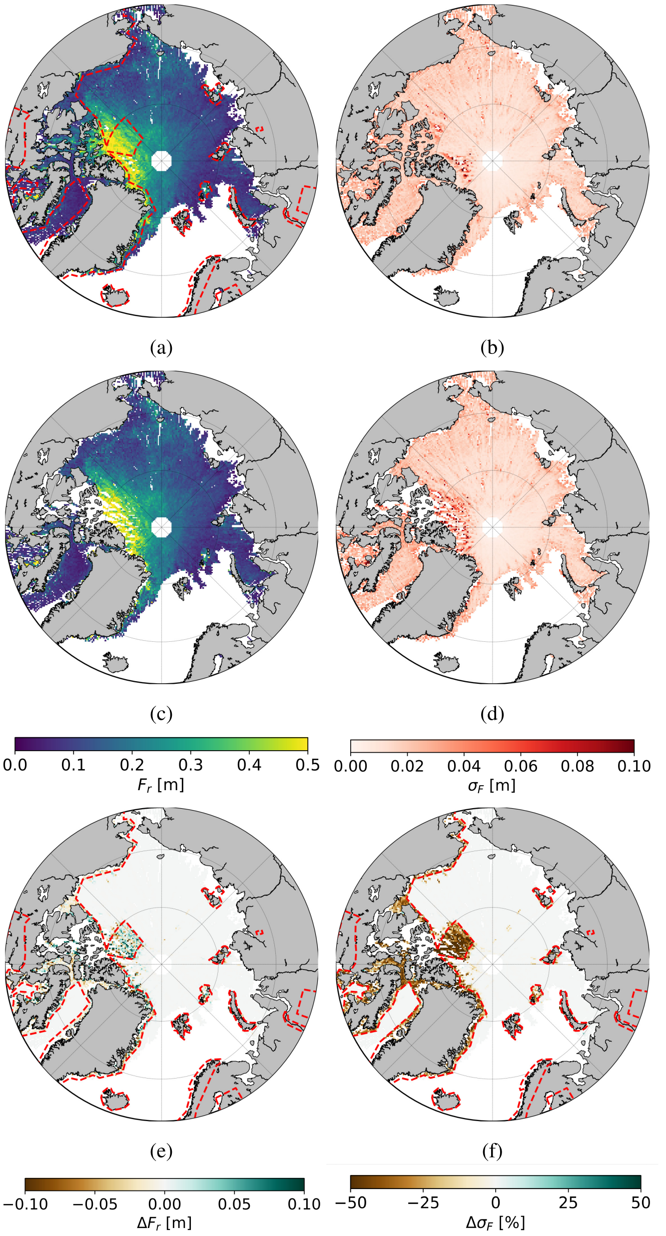

(a) (b)

(c) (d)

(e) (f)

Fig. 9. Arctic gridded radar freeboard (F_r) and random uncertainty (σ_F) for March 2014 from (a) and (b) DTU-MPP and (c) and (d) DTU-SARP. (e) is the difference (a)–(c), and (f) represents the percentage of variation of (b) with respect to (d). Red dashed lines represent the boundaries of the CS2 SARIn acquisition mask.

of sea ice. It has to be noticed that the number of multi-peaked waveforms used by the current version of DTU-MPP does not necessarily reflect the number of leads in a specific region, and it is not used in this study to infer their spatial distribution. While a larger number of multi-peaked waveforms could potentially be included in the processing (see Section V), the relatively low amount of multi-peaked waveforms used in this work does influence CS2 freeboard retrievals, as discussed in Sections IV-B and IV-C.

The distribution of the absolute value of across-track distance for both sea ice and lead peaks for March 2014 is shown in Fig. 8. By including subsequent peaks of SARIn waveforms,

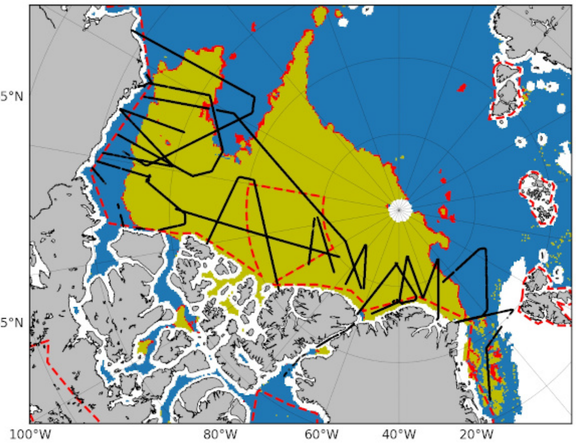

Fig. 10. OIB flight tracks (black lines) acquired between March 12 and 31, 2014, plotted on top of the OSI SAF sea ice type indicating FYI in blue, MYI in yellow, and ambiguous ice type in red. Red dashed line represents the boundaries of the CS2 SARIn acquisition mask valid for spring 2014, including the Wingham Box in the Lincoln Sea.

returns from off-nadir leads are detected up to 4 km across track [see Fig. 8(a)], corresponding to ONC values up to ~12 m—as illustrated in Fig. 8(c), where theoretical values of ONC are plotted as a function of across-track distance following (7) and (8). It is interesting to notice that the average absolute across-track distance of returns originating from sea ice is 111 m [see Fig. 8(b)], corresponding to an ONC of 1.8 cm [see Fig. 8(d)]. This result suggests that including the phase difference available in the CS2 product could potentially correct for biases introduced by empirical threshold retrackers not only for sea surface, as observed in [15], but also for sea ice elevations. While the impact of the chosen retracking threshold on sea ice freeboard and thickness estimates in the Arctic Ocean is discussed, in detail, in [13], this method would be able to correct for retracker-dependent biases on individual measurement points.

B. Impact Assessment and Validation

Results from DTU-MPP for the period January–April 2014 are compared with those from a regular SAR processing scheme, in which SARIn waveforms are processed exactly as SAR waveforms. This processor, referred to as DTU-SARP in the following analysis, only retracks the first peak of SARIn waveforms, does not use the phase information available in the SARIn product, and discards SARIn waveforms with $0.10 < \mathrm{PP} < 0.25$—as considered to be affected by off-nadir ranging. This makes it possible to compare values of freeboard and uncertainty between processors, as they are computed in a consistent way and using similar assumptions, and assess the effect of the proposed multi-peak algorithm on radar freeboard estimates in the Arctic. SAR waveforms are processed in the same way by both DTU-MPP and DTU-SARP.

The radar freeboard estimates and the associated uncertainty maps for March 2014 from the DTU-MPP and the DTU-SARP processors are shown in Fig. 9, together with the difference DTU-MPP−DTU-SARP. As expected, in areas where SIRAL operates in SAR mode, freeboard and uncertainty estimates from both processors have the same value [see Fig. 9(e) and (f)]—apart from some fluctuations at the SARIn mask boundaries caused by the along-track interpolation of the SSA across acquisition modes. The difference DTU-MPP−DTU-SARP in Fig. 9(e) does not highlight any particular spatial pattern. The gridded random radar freeboard uncertainties in Fig. 9(b) and (d) show a latitude-dependent gradient associated with the density of measurements in a grid cell—where the uncertainty decreases with the square root of the number of valid freeboard estimates in a grid cell (see Appendix A). For this reason, the uncertainty increases at the ice edges, where a small number of freeboard retrievals is available, as well as in the Lincoln Sea for DTU-SARP, due to the large number of snagged waveforms that are discarded. As a result of the higher number of freeboard estimates per grid cell, the map in Fig. 9(f) shows a significant reduction of the DTU-MPP random gridded uncertainty compared with the DTU-SARP processor within the SARIn acquisition mask. Maps of the freeboard and uncertainty variations for the months of January, February, and April 2014 are not included here as they show very similar behavior.

The statistics for SARIn regions for the period January–April 2014 are reported in Table II and show that processing multiple peaks of SARIn waveforms does not

TABLE II

AVERAGE RADAR FREEBOARD (F_r), ASSOCIATED RANDOM UNCERTAINTY (σ_F), NUMBER OF LEAD MEASUREMENTS (N_l), AND NUMBER OF VALID FREEBOARD RETRIEVALS (N_F) FROM THE DTU-MPP AND DTU-SARP ALGORITHMS. FREEBOARD AND UNCERTAINTIES ARE EXPRESSED IN cm AND VARIATIONS REFERS TO DTU-MPP−DTU-SARP

		SARIn areas		
		DTU-MPP	**DTU-SARP**	**Variation**
Jan	$\mathbf{F_r}$	21.3	22.3	−1.0
	$\boldsymbol{\sigma_F}$	2.2	3.3	−33%
	$\mathbf{N_l}$	72592	48608	149%
	$\mathbf{N_F}$	400666	186785	215%
Feb	$\mathbf{F_r}$	22.6	23.0	−0.4
	$\boldsymbol{\sigma_F}$	2.3	3.5	−34%
	$\mathbf{N_l}$	66047	41967	157%
	$\mathbf{N_F}$	402099	138959	289%
Mar	$\mathbf{F_r}$	22.1	22.6	−0.5
	$\boldsymbol{\sigma_F}$	2.2	3.5	−37%
	$\mathbf{N_l}$	66597	42463	157%
	$\mathbf{N_F}$	475862	144664	329%
Apr	$\mathbf{F_r}$	22.5	22.6	−0.1
	$\boldsymbol{\sigma_F}$	2.4	3.5	−31%
	$\mathbf{N_l}$	58281	36552	159%
	$\mathbf{N_F}$	404880	149183	271%
Mean	$\mathbf{F_r}$	22.1	22.6	**−0.5**
	$\boldsymbol{\sigma_F}$	2.3	3.5	**−34%**
	$\mathbf{N_l}$	65879	42398	**155%**
	$\mathbf{N_F}$	420877	154898	**272%**

introduce any significant bias on the mean radar freeboard. Differences between monthly averages of DTU-MPP and DTU-SARP freeboard estimates range from 0.1 to 1 cm, with an average of 0.5 cm (subcentimeter freeboard and uncertainty estimates are retained just to investigate differences between the processors). On the other hand, retracking several peaks of SARIn waveforms contributes to a substantial average reduction of ∼34% of the gridded random freeboard uncertainty—between 31% and 37% for the analyzed period. This reduction is attributed to the average 55% larger amount of lead measurements performed in SARIn areas by DTU-MPP compared with DTU-SARP, which has the effect of reducing the average point uncertainty of the SSA and, in turn, the average point uncertainty of the freeboard estimates [15], [17]. The capability of DTU-MPP to provide lead heights in regions where no leads are detected close to the satellite nadir has the additional effect of increasing the number of valid freeboard estimates, i.e., estimates within 100 km from the closest lead height (see Section III-E), inside a grid cell. Table II shows that DTU-MPP provides almost three times (272%) the number of freeboard estimates as DTU-SARP in SARIn areas. If the systematic contributions from the snow depth and snow density are included in the error budget according to Appendix B, the mean 34% reduction of the gridded random freeboard uncertainty observed in the period January–April 2014 equals a reduction in the total sea ice thickness uncertainty from 41 to 33 cm, i.e., about 20%. The reductions in the uncertainty mentioned so far are achieved by comparing the DTU-MPP with the DTU-SARP algorithms, i.e., a multi-peak retracker using the CS2 SARIn phase information with a single-peak retracker not using the phase information—the latter emulating a regular SAR processing scheme. If a simplified version of DTU-MPP, retracking only the first peak of waveforms but using the SARIn phase information in a similar way as in [17], is compared with the DTU-SARP processor, a 17% average gridded random uncertainty reduction is achieved. This means that retracking multiple peaks of SARIn waveforms can double the reduction of the gridded random uncertainty with respect to a single-peak retracker using the SARIn phase information.

Radar freeboard from the DTU-MPP and the DTU-SARP processors is additionally compared with airborne measurements from the OIB campaign acquired between March 12 and 31, 2014 (flight tracks are illustrated in Fig. 10). OIB sea ice freeboard estimates are converted to radar freeboard by inverting (11) and using a constant snow density of 320 kg/m^3 [49]. Positive values of satellite and airborne radar freeboard are averaged to the same EASE 25-km grid (see Appendix A). The correlation r_{F_r} and mean deviation of the satellite freeboard from the airborne freeboard ΔF_r are reported in Table III, together with the number of grid cells N_c used in the comparison.

A ∼0.7 correlation is found between the satellite and airborne freeboard estimates using all available OIB data—comparable to the sea ice thickness correlations found in similar studies, e.g., [7], [8]—showing that both DTU-MPP and DTU-SARP capture well the spatial gradient of freeboard in the study region. With a mean deviation of 3.7 ± 9.6 cm and 2.7 ± 9.4 cm from OIB freeboard estimates, DTU-MPP and DTU-SARP show similar performance in terms of accuracy and precision. In order to assess the impact of the DTU-MPP processing scheme, the same analysis is performed using only grid cells where SIRAL operates in SARIn mode. In SARIn areas, the mean deviation of the satellite freeboard from OIB estimates is 9.8 ± 12.2 cm and 9.2 ± 13.2 cm for DTU-MPP and DTU-SARP, respectively, with a 0.6-cm difference between the two processors. These results show that retracking several peaks of SARIn waveforms, together with the associated phase information, does not introduce any significant bias on freeboard estimates while slightly increasing the precision (standard deviation of the differences) compared with a single-peak processing scheme in which the phase information is not used. At the same time, the proposed algorithm increases the spatial coverage—141 versus 93 grid cells used by DTU-MPP and DTU-SARP, respectively—and the correlation—0.53 for DTU-MPP and 0.32 for DTU-SARP. The absolute accuracy of CS2 freeboard heights with respect to OIB estimates is further discussed in Section IV-C.

TABLE III

COMPARISON OF SATELLITE RADAR FREEBOARD (DTU-MPP, DTU-SARP, AWI, AND JPL) WITH AIRBORNE ESTIMATES (OIB) FOR THE PERIOD MARCH 12–31, 2014. r_{F_r} IS THE CORRELATION, ΔF_r IS THE MEAN DIFFERENCE CS2−OIB IN cm, AND N_c IS THE NUMBER OF GRID CELLS USED IN THE COMPARISON

All OIB data				
	DTU-MPP	**DTU-SARP**	**AWI**	**JPL**
$\mathbf{r_{F_r}}$	0.73	0.69	0.75	0.69
$\mathbf{\Delta F_r}$	3.7 ± 9.6	2.7 ± 9.4	2.9 ± 8.8	−5.5 ± 6.6
$\mathbf{N_c}$	610	568	605	369
SARIn areas				
$\mathbf{r_{F_r}}$	0.53	0.32	0.50	0.55
$\mathbf{\Delta F_r}$	9.8 ± 12.2	9.2 ± 13.2	9.2 ± 10.3	−7.6 ± 6.0
$\mathbf{N_c}$	141	93	114	29

C. Comparison With External Products

In order to investigate the impact of the proposed algorithm on the accuracy of freeboard heights, point estimates of CS2 radar freeboard from the Alfred Wegener Institute's CS2 sea ice product L2i, v2.1 (AWI) [13] and the estimates produced by Dr. Kwok at the NASA Jet Propulsion Laboratory (JPL) are also compared with OIB measurements (see Table III). Again, subcentimeter values are used just to show differences among the processors. It has to be noticed that both the AWI and JPL products do not use the phase information available in the SARIn product and retrack only the first peak of waveforms. The following analysis focuses on values of radar freeboard, as the three satellite products—DTU-MPP, AWI, and JPL—use different assumptions for snow depths and densities in the conversion of radar freeboard to sea ice freeboard.

DTU-MPP, AWI, and JPL show, respectively, 9.8±12.2 cm, 9.2 ± 10.3 cm, and −7.6 ± 6 cm mean deviation from OIB

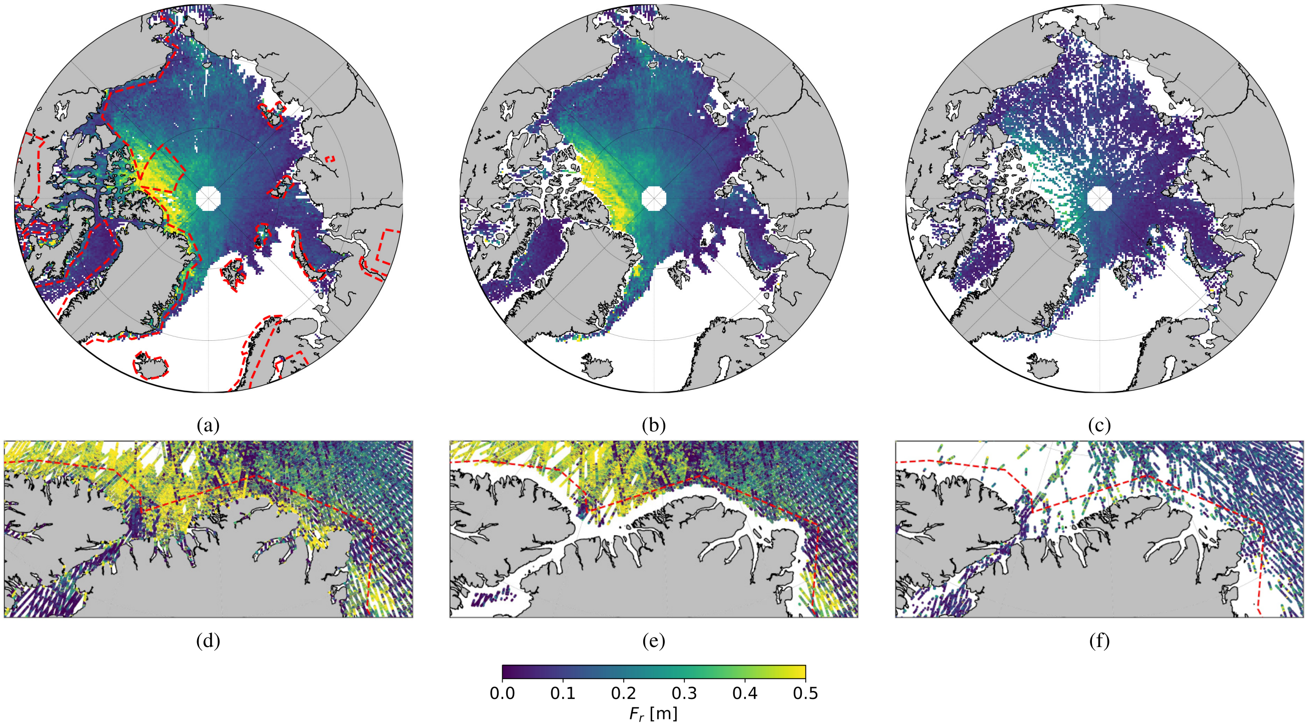
(a) (b) (c)

(d) (e) (f)

Fig. 11. Arctic gridded radar freeboard estimates from (a) DTU-MPP, (b) AWI, and (c) JPL processors. (d)–(f) show the point estimates of radar freeboard and the spatial coverage of the three products—DTU-MPP, AWI, and JPL, respectively—in the coastal domain north of Greenland and Ellesmere Island. Red dashed lines represent the boundaries of the CS2 SARIn acquisition mask.

estimates in SARIn regions, with JPL freeboards being the closest to OIB. The large difference between DTU-MPP/AWI and JPL estimates is likely due to the different retrackers used to estimate surface heights. While DTU-MPP and AWI use a similar algorithm, retracking the 50% power point on the waveforms leading edge, JPL estimates are obtained with a retracker that takes the centroid of the waveform area as the retracking point [8]. Such retracker has been shown in [33] to be less sensitive to the scattering from the air/snow interface, which, due to SIRAL's range resolution of ~46 cm, can cause a broadening of the leading edge of CS2 waveforms and an overestimation of sea ice elevations. Simulations performed in [33] estimate this effect to be larger in regions with snow thicknesses above 20 cm. This is likely to be the reason for the lower freeboard estimates from the JPL data set compared with DTU-MPP and AWI since a large amount of OIB measurements inside the CS2 SARIn acquisition mask are performed over MYI (see Fig. 10), which carries thicker snow load than FYI. Thus, the accuracy of freeboard estimates in this analysis is mainly determined by the kind of retracker used. For this reason, an increase in the accuracy of freeboard estimates from DTU-MPP over those from DTU-SARP is not necessarily expected in this kind of comparison, as the dominant elevation bias is likely to be caused by the snow-related broadening of the waveform leading edge and not by off-nadir scattering—which the DTU-SARP processor tries to limit by discarding waveforms with specific values of PP (see Section IV-B). The higher precision of the JPL and AWI products compared with DTU-MPP—i.e., the lower standard deviation of the differences in Table III—is also due to the different processing techniques used by the processors. Even if the retracker used by AWI and DTU-MPP is similar, the AWI processor smooths CS2 waveforms before retracking and uses a 100-km moving window to smooth the along-track SSA [Hendricks, personal communication] compared with the 25-km window used by DTU-MPP.

The JPL product uses a more conservative classification algorithm that discards many waveforms, especially in the MYI regions. This can be observed in the number of grid cells used for the comparison, which, for the SARIn regions, counts 141 and 114 for DTU-MPP and AWI, respectively, while only 29 for JPL. The spatial coverage of the three products can be observed in Fig. 11. DTU-MPP and AWI provide a larger amount of freeboard estimates compared with JPL in the entire Arctic basin [see Fig. 11(a)–(c)], especially over the thick MYI north of Greenland. Fig. 11(d)–(f) shows the point freeboard estimates from the three products along the northern coast of Greenland and Ellesmere Island. The slightly higher coverage of the AWI product compared with DTU-MPP in SAR regions, i.e., above the red dashed line, is likely due to AWI's processor discarding freeboard estimates further than 200 km from the closest lead [Hendricks, personal communication], as opposed to DTU-MPP that uses a 100-km threshold. DTU-MPP shows an overall increased spatial coverage in SARIn regions, especially below ~30 km from the coast. While the AWI product does not provide freeboard estimates in this areas due to the lack of valid sea ice concentration estimates in the OSI SAF product along the coast, DTU-MPP will always provide a larger number of valid measurements in coastal regions where SIRAL operates in SARIn mode compared with regular SAR processing schemes. This is due to the ability to deal with off-nadir scattering from land and, therefore, to better cope with footprint contamination, as shown in [50]. The latter is especially true in regions with sharp transitions between ocean and land, e.g., Northern Greenland and the Canadian Archipelago, where ONC-corrected heights enable to easily distinguish between the two kinds of surfaces.

V. DISCUSSION

Returns from Arctic sea ice in the analyzed regions are retracked at an average distance of 111 m from the subsatellite point, leading to an equivalent average ONC correction of 1.8 cm for sea ice elevations. In previous work by [15], [17], the ONC was applied only to lead elevations as, due to the geometry of relatively flat areas, such as the Arctic Ocean, returns over sea ice should originate almost at the satellite nadir and the respective ONC should be negligible for sea ice elevations. However, these results show that, when using a 50% threshold retracker, the across-track location corresponding to the waveform retracking point slightly deviates, on average, from the satellite nadir. This confirms that threshold-based empirical retrackers might not always pick a point on the waveform corresponding to the exact satellite nadir, as the location of this point is influenced by surface roughness at the footprint scale [33], [51], [52]. Point estimates of sea ice freeboard obtained from ONC-corrected elevations are, therefore, likely to be always more accurate than uncorrected estimates, as the ONC takes care of biases introduced by empirical retrackers [15].

The magnitude of the improvement brought by the ONC with respect to sea ice freeboard estimates depends strongly on the chosen waveform classification and retracking algorithms and needs a more detailed discussion. The impact of the ONC might be less significant when selecting in a very conservative way the waveforms to be processed. For instance, by choosing only extremely strong returns from leads close to the satellite nadir, Armitage and Davidson [15] found an average -1.2 cm bias in the SSH, which would contrast the average -1.8 cm bias found in this work for sea ice elevations using a 50% threshold retracker. Furthermore, the results in Section IV-C show that the retracking algorithm plays a major role in determining the accuracy of CS2 sea ice elevations, especially in areas with a thick snow layer. Thus, when comparing sea ice processing schemes based on different classification and retracking algorithms, the benefits of the ONC on the accuracy of area-averaged estimates of sea ice freeboard might not always be notable. On the other hand, conservative waveform selection algorithms might lead to the rejection of a large amount of CS2 data and more sparse availability of freeboard estimates in the Arctic (see Fig. 11). This work shows how using the CS2 SARIn information to compute the ONC and retracking several peaks of SARIn waveforms enables to process most of the measurements usually discarded in regular altimetry processing schemes. This increases significantly the geographical availability of freeboard heights—e.g., about five times larger compared with the JPL product—without affecting the final accuracy of the estimates—compared with the DTU-SARP processor, which neither relies on multi-peak retracking nor uses the SARIn phase information. Several studies show that physical retrackers increase the accuracy of sea ice freeboard estimates by taking into account surface roughness [51]–[53] although no currently existing physical model can account for multi-peaked waveforms. Future assessments of the accuracy of empirical retracking algorithms should include the use of adaptive thresholds based on surface roughness values—i.e., for leads and different kinds of sea ice—or apply a roughness-dependent correction, as suggested by [53].

The accuracy and the precision of SSH estimates would instead always benefit from the application of the ONC, as this correction both accounts for retracker-dependent biases, and it increases the number of available SSH retrievals compared with regular SAR altimetry [15]. The multi-peak processing scheme proposed in this work further increases the number of lead measurements by including returns originating far from the main waveform peak, i.e., far from the subsatellite point. This provides SSH measurements in areas where a regular single-peak retracker, even using the SARIn phase information as those used in [15] and [17], would not. Retracking several peaks of SARIn waveforms in combination with a high-resolution coastline would therefore provide a more dense and accurate sampling of the winter SSH in coastal areas and in ice-covered regions, with the potential to provide SSH measurements from leads located at less than 1 km from the coast. This has clear implications for MSS products—mostly relying on geoid heights in the coastal domain—as well as tide models based on altimetry measurements—where the across-track relocation of measurements and the high-resolution coastline can aid the detection of footprints contaminated by land. More accurate MSS products and tidal corrections would, in turn, improve altimetry-based freeboard and thickness retrievals. A more thorough validation of both SSH and freeboard estimates is, however, needed in coastal regions, where the time difference between the acquisition of CS2 and the validation data plays a major role due to the scarce availability of coastal sea ice drift products, as well as by, sometimes, very rapid ice dynamics occurring along the coast.

The multi-peak retracking algorithm discussed in this work is based on the assumption that off-nadir returns from subsequent peaks, i.e., occurring to the right of the first and main waveform peak, only originate from leads. For this reason, an empirical threshold of ±15 cm from the reference along-track SSA is used to choose suitable subsequent peaks (see Section III-E). While both the analysis of several optical coincident images (an example in Section IV-A) and the good agreement between DTU-MPP and DTU-SARP freeboard estimates (see Section IV-B) support this assumption, further investigation on a larger scale should be carried out to study the origin of far off-nadir returns. When some of these returns originate instead from, e.g., rough patches of sea ice or large ridges, a different classification algorithm should be developed. The ±15-cm threshold also sets the amount of processed multi-peaked waveforms as the $\sim$2% of the available SARIn measurements in a month (see Section IV-A). In this study, another ~8% of the waveforms shows more than one distinct peak associated with actual ground features visible in optical images, but most of the peaks are discarded based on their retracked elevation. Potentially, a larger number of peaks might be included in the processing by testing different retrackers—perhaps physical retrackers taking into account surface roughness and volume scattering in combination with the available phase information—providing more accurate elevations for the subsequent peaks. The number of usable peaks might be further increased also by testing lower coherence thresholds—this work selects peaks with a coherence over 0.9 as opposed to the 0.7 threshold used in [15]—or by developing more sophisticated peak classification algorithms not only based on the deviation from a reference along-track SSA.

The current CS2 SARIn coverage of the Arctic Ocean is relatively scarce and, since CS2 started operating in SAR mode also inside the Wingham box in October 2014, limited to coastal areas. Besides the aforementioned improvements and potential for coastal regions, this work shows that the multi-peak retracking algorithm strongly benefits sea ice freeboard estimation inside the Wingham box too and over both FYI and MYI. The multi-peak approach could potentially be applied also in the ice-covered Southern Ocean. In fact, the highly fragmented nature of the Antarctic sea ice cover, continuously subjected to divergent motion [54], offers a large amount of off-nadir returns that cannot be used by regular SAR altimetry processing schemes. Furthermore, the increased amount of measurements provided by multi-peak retracking would be especially beneficial in the Southern Ocean due to the lower CS2 track density over sea ice than in the Arctic—a large amount of Antarctic sea ice is located between 55 and 70°S [55], as opposed to the majority of Arctic sea ice that lies between 70 and 90°N.

All these results suggest that future satellite radar altimetry missions operating in SARIn mode over the entirety of both Earth's polar regions have the potential to increase the accuracy and significantly reduce the uncertainty of sea ice thickness estimates.

VI. CONCLUSION

This work proposes an algorithm (DTU-MPP) capable of retracking multiple peaks of CS2 L1b SARIn waveforms over Arctic sea ice, exploiting the phase information available in this acquisition mode. The objective of the analysis is to validate the methodology and assess the potential of this technique with respect to the estimation of sea ice freeboard and thickness in the Arctic Ocean.

It is found that retracking multiple peaks, in combination with the respective phase information, enables us to obtain more than one valid height estimate from single SARIn waveforms over sea ice. In particular, subsequent coherent peaks of SARIn waveforms are observed to correspond to surface features visible in several coincident satellite optical images, with returns detected up to 4 km across the track. This work assumes all subsequent coherent peaks to originate from off-nadir leads although further investigation should aim to validate this assumption using, e.g., additional SARIn data and coincident satellite imagery in a way similar to [56].

Using a 50% threshold retracker, sea ice returns are retracked at an average across-track distance of 111 m from the satellite nadir, corresponding to an average elevation bias of −1.8 cm. The SARIn phase information can be used to correct for this retracker-dependent bias on individual measurement points. The sea ice elevation bias might not affect significantly the accuracy of sea ice freeboard estimated by choosing only strong lead returns originating at the satellite nadir, where a similar average −1.2-cm bias has been estimated for lead elevations [15]. However, conservative waveform selection algorithms discard a large amount of data.

Compared with a regular SAR processing scheme retracking single peaks and not using the SARIn phase information (DTU-SARP), the proposed multi-peak retracking algorithm provides an average 55% increase in the number of SSH measurements in ice-covered regions and a 2.7-fold increase in the number of valid freeboard retrievals, between January and April 2014. Assuming the error contributions to be uncorrelated and independent, this has the effect to reduce on average the gridded random freeboard uncertainty by ~34%, which corresponds to a ~20% reduction of the total sea ice thickness uncertainty, when the systematic contributions from the snow depth and the snow density are included in the error budget.

In March 2014, DTU-MPP is shown to increase the correlation between CS2 freeboard and OIB airborne estimates from 0.32 to 0.53 in SARIn regions compared with DTU-SARP. The proposed methodology does not introduce a bias on the freeboard estimates, while it slightly increases their precision with respect to OIB data. At the same time, DTU-MPP covers an area about five times larger than the JPL product, which is based on a more conservative waveform selection algorithm.

Due to the current scarce SARIn coverage of the Arctic Ocean, DTU-MPP would bring improvements mostly in the coastal domain, where CS2 still operates in SARIn mode. The phase information, in combination with a high-resolution coastline, can be successfully used to discard echoes contaminated by scattering from land and provide a more dense sampling of the SSH during the winter season. This would improve MSS products, which currently includes very few SSH estimates in ice-covered regions, as well as tide models relying on altimetry measurements, with significant benefits for the retrieval of a large variety of geophysical quantities from altimetry. Further investigation should aim to perform a more thorough validation of both freeboard and SSH estimates in coastal regions, using coincident airborne and *in situ* measurements.

The multi-peak retracking algorithm also shows a good potential for applications in the Southern Ocean, where the fragmented nature of the Antarctic sea ice cover provides a large amount of off-nadir returns, which cannot be used by regular SAR processing schemes. The CS2 SARIn mode, on the other hand, would allow correcting for off-nadir ranging for each individual sea ice and ocean elevation in the Southern Ocean too. The results presented and discussed in this work suggest that future satellite radar altimetry missions operating in SARIn mode over the entire polar regions—e.g., the ESA candidate mission CRISTAL—would provide a denser sampling of the SSH and the sea ice thickness, in addition to more precise and accurate estimates in ice-covered regions [15], than the SAR mode.

APPENDIX A
GRIDDING

For N measurements of a variable x, the representative value in each grid cell, i.e., the average $\overline{x}$, is computed using the weighted average

$$\overline{x} = \frac{\sum_{i=0}^{N} w_i x_i}{\sum_{i=0}^{N} w_i} \tag{17}$$

where w_i is the weight of each measurement, defined as the inverse of the squared point uncertainty σ_{x_i}

$$w_i = \frac{1}{\sigma_{x_i}^2}. \tag{18}$$

Because the weighted average $\overline{x}$ is a function of the original measured values $x_1, x_2, \ldots, x_N$, the uncertainty in $\overline{x}$ can be calculated using error propagation [57]

$$\sigma_{\overline{x}} = \frac{1}{\sqrt{\sum_{i=0}^{N} w_i}}. \tag{19}$$

APPENDIX B
SEA ICE THICKNESS AND THICKNESS UNCERTAINTY

By assuming the sea ice in hydrostatic equilibrium with the surrounding water, point estimates of sea ice thickness T can be estimated from the sea ice freeboard following [5] as:

$$T = F_i \frac{\rho_w}{\rho_w - \rho_i} + h_s \frac{\rho_s}{\rho_w - \rho_i} \tag{20}$$

where ρ_w, ρ_i, and ρ_s are the density of water, sea ice, and snow, respectively. During winter, water density can vary between about 1024 and 1027 kg/m^3 [58], while ice density can vary significantly depending on the method used to estimate it [59]. In this study, a fixed water density of 1025 kg/m^3 and ice densities of 917 and 882 kg/m^3 for FYI and MYI, respectively, are used in the freeboard to thickness conversion. These values are based on *in situ* ice and snow data from 689 observation sites, obtained during the Sever expeditions in the 1980s and reported by [59].

The total uncertainty of the sea ice thickness at each measurement location σ_T is computed using the Gaussian propagation of the uncertainty on (20) as

$$\begin{aligned}\sigma_T^2 &= \left(\frac{\partial T}{\partial F_i}\right)^2 \sigma_{F_i}^2 + \left(\frac{\partial T}{\partial \rho_i}\right)^2 \sigma_{\rho_i}^2 + \left(\frac{\partial T}{\partial h_s}\right)^2 \sigma_{h_s}^2 \\ &\quad + \left(\frac{\partial T}{\partial \rho_s}\right)^2 \sigma_{\rho_s}^2 \\ &= \left(\frac{\rho_w}{\rho_w - \rho_i}\right)^2 \sigma_{F_i}^2 + \left(\frac{\rho_w F_i + \rho_s h_s}{(\rho_w - \rho_i)^2}\right)^2 \sigma_{\rho_i}^2 \\ &\quad + \left(\frac{\rho_s}{\rho_w - \rho_i}\right)^2 \sigma_{h_s}^2 + \left(\frac{h_s}{\rho_w - \rho_i}\right)^2 \sigma_{\rho_s}^2\end{aligned} \tag{21}$$

where the negligible contribution due to variations in sea water density is not included in the estimation [49]. The uncertainty of the ice density σ_{ρ_i} is taken in this study as 35 and 23 kg/m^3 for FYI and MYI, respectively, from [59], while the uncertainty of the sea ice freeboard σ_{F_i} can be estimated from the radar freeboard uncertainty σ_{F_r} by combining (14), (15), and (16) as

$$\sigma_{F_i}^2 = \sigma_{F_r}^2 + \left(\frac{c}{c_s} - 1\right)^2 \sigma_{h_s}^2 + \left(-\frac{h_s c}{c_s^2}\right)^2 \sigma_{c_s}^2 \tag{22}$$

with

$$\sigma_{c_s} = -\frac{c(14\rho_s + 17)}{20\left(7/10\rho_s^2 + 17/10\rho_s + 1\right)^{3/2}} \sigma_{\rho_s}. \tag{23}$$

In (21), (22), and (23), the uncertainties of the snow depth σ_{h_s} and density σ_{ρ_s} are provided by the W99 climatology. As for the sea ice freeboard, these uncertainty contributions are considered to be systematic so that the random part of the sea ice thickness uncertainty is approximated in this study by the first two terms of (21). The gridded random thickness uncertainty is obtained according to Appendix A. When discussing the total uncertainty of gridded thickness estimates in Section IV-B, the average systematic error contributions from snow depth and density are added in quadrature to the random part of the uncertainty for every grid cell.

ACKNOWLEDGMENT

The CryoSat-2 Full Bit Rate SARIn data for the period January–April 2014 were processed by Dr. Scagliola at Aresys S.r.l., who provided the level 1b product utilized in this work. The processing of the CryoSat-2 sea ice thickness by the Alfred Wegener Institute is funded by the German Ministry of Economics Affairs and Energy under Grant 50EE1008, and the data are available at https://www.meereisportal.de under Grant REKLIM-2013-04. The level 2i product used in this study was kindly provided by Dr. Hendricks. The OpenStreetMapData project is based on OpenStreetMap data (OpenStreetMap contributors) and available under the Open Data Commons Open Database License (ODbL).

REFERENCES

[1] J. A. Curry, J. L. Schramm, and E. E. Ebert, "Sea ice-albedo climate feedback mechanism," *J. Climate*, vol. 8, no. 2, pp. 240–247, Feb. 1995.

[2] P. Wadhams, "Sea ice thickness changes and their relation to climate," in *The Polar Oceans and Their Role in Shaping the Global Environment*. Washington, DC, USA: American Geophysical Union (AGU), 2013, pp. 337–361.

[3] K. Aagaard and E. C. Carmack, "The role of sea ice and other fresh water in the Arctic circulation," *J. Geophys. Res., Oceans*, vol. 94, no. 10, pp. 14485–14498, 1989.

[4] F. T. Ulaby, R. K. Moore, and A. K. Fung, *Microwave Remote Sensing: Active and Passive. Vol. 3: From Theory to Applications*, vol. 3. Norwood, MA, USA: Artech House, 1986.

[5] S. Laxon, N. Peacock, and D. Smith, "High interannual variability of sea ice thickness in the Arctic region," *Nature*, vol. 425, no. 6961, pp. 947–950, Oct. 2003.

[6] R. Kwok, G. F. Cunningham, M. Wensnahan, I. Rigor, H. J. Zwally, and D. Yi, "Thinning and volume loss of the Arctic ocean sea ice cover: 2003–2008," *J. Geophys. Res., C, Oceans*, vol. 114, no. 7, 2009, Art. no. C07005.

[7] S. W. Laxon *et al.*, "CryoSat-2 estimates of Arctic sea ice thickness and volume," *Geophys. Res. Lett.*, vol. 40, no. 4, pp. 732–737, 2013.

[8] R. Kwok and G. F. Cunningham, "Variability of Arctic sea ice thickness and volume from CryoSat-2," *Phil. Trans. Roy. Soc. London A, Math., Phys. Eng. Sci.*, vol. 373, no. 2045, 2015, Art. no. 20140157.

[9] T. W. K. Armitage and A. L. Ridout, "Arctic sea ice freeboard from AltiKa and comparison with CryoSat-2 and operation icebridge," *Geophys. Res. Lett.*, vol. 42, no. 16, pp. 6724–6731, 2015.

[10] R. L. Tilling, A. Ridout, and A. Shepherd, "Estimating Arctic sea ice thickness and volume using CryoSat-2 radar altimeter data," *Adv. Space Res.*, vol. 62, no. 6, pp. 1203–1225, Sep. 2018.

[11] D. J. Wingham *et al.*, "CryoSat: A mission to determine the fluctuations in Earth's land and marine ice fields," *Adv. Space Res.*, vol. 37, no. 4, pp. 841–871, 2006.

[12] K. A. Giles *et al.*, "Combined airborne laser and radar altimeter measurements over the fram strait in May 2002," *Remote Sens. Environ.*, vol. 111, nos. 2–3, pp. 182–194, Nov. 2007.

[13] R. Ricker, S. Hendricks, V. Helm, H. Skourup, and M. Davidson, "Sensitivity of CryoSat-2 Arctic sea-ice freeboard and thickness on radar-waveform interpretation," *Cryosphere*, vol. 8, no. 4, pp. 1607–1622, Aug. 2014.

[14] R. K. Raney, "The delay/Doppler radar altimeter," *IEEE Trans. Geosci. Remote Sens.*, vol. 36, no. 5, pp. 1578–1588, Sep. 1998.

[15] T. W. K. Armitage and M. W. J. Davidson, "Using the interferometric capabilities of the ESA CryoSat-2 mission to improve the accuracy of sea ice freeboard retrievals," *IEEE Trans. Geosci. Remote Sens.*, vol. 52, no. 1, pp. 529–536, Jan. 2014.

[16] F. M. Fetterer, M. R. Drinkwater, K. C. Jezek, S. W. C. Laxon, R. G. Onstott, and L. M. H. Ulander, "Sea ice altimetry," in *Microwave Remote Sensing of Sea Ice*. Washington, DC, USA: American Geophysical Union, 1992.

[17] A. Di Bella, H. Skourup, J. Bouffard, and T. Parrinello, "Uncertainty reduction of Arctic sea ice freeboard from CryoSat-2 interferometric mode," *Adv. Space Res.*, vol. 62, no. 6, pp. 1251–1264, Sep. 2018.

[18] L. Gray *et al.*, "Interferometric swath processing of CryoSat data for glacial ice topography," *Cryosphere*, vol. 7, no. 6, pp. 1857–1867, Dec. 2013.

[19] L. Foresta, N. Gourmelen, F. Pálsson, P. Nienow, H. Björnsson, and A. Shepherd, "Surface elevation change and mass balance of Icelandic ice caps derived from swath mode CryoSat-2 altimetry," *Geophys. Res. Lett.*, vol. 43, no. 23, pp. 12138–12145, 2016.

[20] N. Gourmelen *et al.*, "CryoSat-2 swath interferometric altimetry for mapping ice elevation and elevation change," *Adv. Space Res.*, vol. 62, no. 6, pp. 1226–1242, Sep. 2018.

[21] C. Bouzinac, "CryoSat product handbook," Eur. Space Agency, Univ. College London, London, U.K., Tech. Rep., 2014.

[22] A. Di Bella, M. Scagliola, L. Maestri, H. Skourup, and R. Forsberg, "Improving CryoSat-2 SARIn L1b products to account for inaccurate phase difference: Impact on sea ice freeboard retrieval," *IEEE Geosci. Remote Sens. Lett.*, vol. 17, no. 2, pp. 252–256, Feb. 2020.

[23] M. Scagliola, M. Fornari, J. Bouffard, and T. Parrinello, "The CryoSat interferometer: End-to-end calibration and achievable performance," *Adv. Space Res.*, vol. 62, no. 6, pp. 1516–1525, Sep. 2018, doi: 10.1016/j.asr.2017.09.024.

[24] M. Meloni *et al.*, "CryoSat ice baseline-D validation and evolutions," *Cryosphere*, vol. 14, no. 6, pp. 1889–1907, Jun. 2020.

[25] N. Kurtz, M. Studinger, J. Harbeck, V. Onana, and D. Yi, "IceBridge L4 sea ice freeboard, snow depth, and thickness, version 1," NASA Nat. Snow Ice Data Center Distrib. Active Arch. Center, Boulder, CO, USA, Tech. Rep., 2015. [Online]. Available: https://nsidc.org/data/IDCSI4/versions/1, doi: 10.5067/G519SHCKWQV6.

[26] V.-D.-P. Onana, N. T. Kurtz, S. L. Farrell, L. S. Koenig, M. Studinger, and J. P. Harbeck, "A sea-ice lead detection algorithm for use with high-resolution airborne visible imagery," *IEEE Trans. Geosci. Remote Sens.*, vol. 51, no. 1, pp. 38–56, Jan. 2013.

[27] V. Ihlen, "Landsat 8 (L8) data users handbook," U.S. Geol. Survey (USGS), Sioux Falls, SD, USA, Nat. Aeronaut. Space Admin. (NASA), Greenbelt, MD, USA, Tech. Rep. 5, Nov. 2019.

[28] R. Tonboe, J. Lavelle, R.-H. Pfeiffer, and E. Howe, "Product user manual for OSI SAF global sea ice concentration. Product OSI-401-b, version is 1.6," Danish Meteorol. Inst., Copenhagen, Denmark, 2017.

[29] P. Wessel and W. H. F. Smith, "A global, self-consistent, hierarchical, high-resolution shoreline database," *J. Geophys. Res., Solid Earth*, vol. 101, no. 4, pp. 8741–8743, Apr. 1996.

[30] J. Nilsson, A. Gardner, L. S. Sørensen, and R. Forsberg, "Improved retrieval of land ice topography from CryoSat-2 data and its impact for volume-change estimation of the greenland ice sheet," *Cryosphere*, vol. 10, no. 6, pp. 2953–2969, Dec. 2016.

[31] G. D. Quartly *et al.*, "Retrieving sea level and freeboard in the Arctic: A review of current radar altimetry methodologies and future perspectives," *Remote Sens.*, vol. 11, no. 7, p. 881, Apr. 2019.

[32] N. Galin, D. J. Wingham, R. Cullen, M. Fornari, W. H. F. Smith, and S. Abdalla, "Calibration of the CryoSat-2 interferometer and measurement of across-track ocean slope," *IEEE Trans. Geosci. Remote Sens.*, vol. 51, no. 1, pp. 57–72, Jan. 2013.

[33] R. Kwok, "Simulated effects of a snow layer on retrieval of CryoSat-2 sea ice freeboard," *Geophys. Res. Lett.*, vol. 41, no. 14, pp. 5014–5020, Jul. 2014.

[34] J. K. Ridley and K. C. Partington, "A model of satellite radar altimeter return from ice sheets," *Int. J. Remote Sens.*, vol. 9, no. 4, pp. 601–624, Apr. 1988.

[35] D. J. Wingham, L. Phalippou, C. Mavrocordatos, and D. Wallis, "The mean echo and echo cross product from a beamforming interferometric altimeter and their application to elevation measurement," *IEEE Trans. Geosci. Remote Sens.*, vol. 42, no. 10, pp. 2305–2323, Oct. 2004.

[36] R. Kwok and J. Morison, "Sea surface height and dynamic topography of the ice-covered oceans from CryoSat-2: 2011–2014," *J. Geophys. Res., Oceans*, vol. 121, no. 1, pp. 674–692, Jan. 2016.

[37] U. Spagnolini, "2-D phase unwrapping and phase aliasing," *Geophysics*, vol. 58, no. 9, pp. 1324–1334, Sep. 1993.

[38] O. Andersen, P. Knudsen, and L. Stenseng, "The DTU13 MSS (mean sea surface) and MDT (mean dynamic topography) from 20 years of satellite altimetry," in *IGFS 2014* (International Association of Geodesy Symposia), S. Jin and R. Barzaghi, Eds. Cham, Switzerland: Springer, 2016, pp. 111–121.

[39] H. Skourup *et al.*, "An assessment of state-of-the-art mean sea surface and geoid models of the Arctic ocean: Implications for sea ice freeboard retrieval," *J. Geophys. Res., Oceans*, vol. 122, no. 11, pp. 8593–8613, Nov. 2017.

[40] S. G. Beaven *et al.*, "Laboratory measurements of radar backscatter from bare and snow-covered saline ice sheets," *Int. J. Remote Sens.*, vol. 16, no. 5, pp. 851–876, Mar. 1995.

[41] R. Willatt, S. Laxon, K. Giles, R. Cullen, C. Haas, and V. Helm, "Ku-band radar penetration into snow cover on Arctic sea ice using airborne data," *Ann. Glaciol.*, vol. 52, no. 57, pp. 197–205, 2011.

[42] R. C. Willatt, K. A. Giles, S. W. Laxon, L. Stone-Drake, and A. P. Worby, "Field investigations of ku-band radar penetration into snow cover on Antarctic sea ice," *IEEE Trans. Geosci. Remote Sens.*, vol. 48, no. 1, pp. 365–372, Jan. 2010.

[43] M. Tiuri, A. Sihvola, E. Nyfors, and M. Hallikaiken, "The complex dielectric constant of snow at microwave frequencies," *IEEE J. Ocean. Eng.*, vol. 9, no. 5, pp. 377–382, Dec. 1984.

[44] S. G. Warren *et al.*, "Snow depth on Arctic sea ice," *J. Climate*, vol. 12, pp. 1814–1829, Jun. 1999.

[45] T. Newman *et al.*, "Assessment of radar-derived snow depth over Arctic sea ice," *J. Geophys. Res., Oceans*, vol. 119, no. 12, pp. 8578–8602, Dec. 2014.

[46] N. T. Kurtz and S. L. Farrell, "Large-scale surveys of snow depth on Arctic sea ice from operation IceBridge," *Geophys. Res. Lett.*, vol. 38, no. 20, pp. 1–5, Oct. 2011.

[47] M. J. Brodzik, B. Billingsley, T. Haran, B. Raup, and M. H. Savoie, "EASE-grid 2.0: Incremental but significant improvements for Earth-gridded data sets," *ISPRS Int. J. Geo-Inf.*, vol. 1, no. 1, pp. 32–45, Mar. 2012.

[48] S. L. Farrell *et al.*, "Mean dynamic topography of the Arctic ocean," *Geophys. Res. Lett.*, vol. 39, no. 1, pp. 1–5, Jan. 2012.

[49] N. T. Kurtz *et al.*, "Sea ice thickness, freeboard, and snow depth products from operation IceBridge airborne data," *Cryosphere*, vol. 7, no. 4, pp. 1035–1056, Jul. 2013.

[50] A. Abulaitijiang, O. B. Andersen, and L. Stenseng, "Coastal sea level from inland CryoSat-2 interferometric SAR altimetry," *Geophys. Res. Lett.*, vol. 42, no. 6, pp. 1841–1847, 2015.

[51] N. T. Kurtz, N. Galin, and M. Studinger, "An improved CryoSat-2 sea ice freeboard retrieval algorithm through the use of waveform fitting," *Cryosphere*, vol. 8, no. 4, pp. 1217–1237, Jul. 2014.

[52] J. C. Landy, A. A. Petty, M. Tsamados, and J. C. Stroeve, "Sea ice roughness overlooked as a key source of uncertainty in CryoSat-2 ice freeboard retrievals," *J. Geophys. Res., Oceans*, vol. 125, no. 5, May 2020.

[53] A. Laforge *et al.*, "Toward improved sea ice freeboard observation with SAR altimetry using the physical retracker SAMOSA+," *Adv. Space Res.*, to be published, doi: 10.1016/j.asr.2020.02.001.

[54] P. R. Holland and R. Kwok, "Wind-driven trends in Antarctic sea-ice drift," *Nature Geosci.*, vol. 5, no. 12, pp. 872–875, Dec. 2012.

[55] P. R. Holland, N. Bruneau, C. Enright, M. Losch, N. T. Kurtz, and R. Kwok, "Modeled trends in Antarctic sea ice thickness," *J. Climate*, vol. 27, no. 10, pp. 3784–3801, May 2014.

[56] A. Wernecke and L. Kaleschke, "Lead detection in Arctic sea ice from CryoSat-2: Quality assessment, lead area fraction and width distribution," *Cryosphere*, vol. 9, no. 5, pp. 1955–1968, Oct. 2015.

[57] J. R. Taylor, *An Introduction to Error Analysis*, vol. 56, 2nd ed. Mill Valley, CA, USA: Univ. Science Books, 1997.

[58] V. K. Pavlov, "Circulation in ice-covered waters," in *Physics of the Ice-Covered Seas*, vol. 2, M. Leppäranta, Ed. Helsinki, Finland: Helsinki Univ. Printing House, 1998, pp. 447–482.

[59] V. Alexandrov, S. Sandven, J. Wahlin, and O. M. Johannessen, "The relation between sea ice thickness and freeboard in the Arctic," *Cryosphere*, vol. 4, no. 3, pp. 373–380, Sep. 2010.

Alessandro Di Bella received the M.Sc. degree in telecommunications engineering from the Politecnico of Milan, Milan, Italy, in 2011, and the M.Sc. degree in Earth and space physics and engineering and the Ph.D. degree in polar remote sensing from the Technical University of Denmark, Kongens Lyngby, Denmark, in 2015 and 2019, respectively.

In 2018, during his Ph.D., he was with the Jet Propulsion Laboratory, Pasadena, CA, USA. He is a Postdoctoral Researcher with the Geodesy and Earth Observation Group, DTU Space, National Space Institute, Technical University of Denmark, Kongens Lyngby. He is a member of CryoSat Scientific Experts Group. His research interests include the monitoring of sea ice in the Arctic Ocean using satellite and airborne remote sensing observations. He took part in several field campaigns in the Arctic, both on land and sea ice, involving the collection of *in situ* measurements as well as airborne radar observations.

Ronald Kwok (Life Fellow, IEEE) received the B.Sc. degree *(summa cum laude)* from Texas A&M University, College Station, TX, USA, in 1976, and the Ph.D. degree from Duke University, Durham, NC, USA, in 1980.

He was a Postdoctoral Fellow with the University of British Columbia, Vancouver, BC, USA. He joined Jet Propulsion Laboratory, Pasadena, CA, USA, in 1985, where he is the Senior Research Scientist. His research interests include the mass and energy balance of the Arctic and Southern Ocean ice cover and the role of the sea ice in global climate, with a focus on the analysis of thickness, small-scale sea ice kinematics, and time-varying gravity from various spaceborne and airborne instruments. He has over 200 referred publications and numerous articles on the state of the polar regions.

Thomas W. K. Armitage received the M.Sc. degree in physics from the Department of Physics, University College London, London, U.K., in 2011, and the Ph.D. degree in polar remote sensing from the Department of Earth Sciences, University College London, in 2016.

From 2011 to 2012 he worked as a Young Graduate Trainee with the European Space Agency, Noordwijk, The Netherlands, on novel interferometric CryoSat-2 retrievals over sea ice. Upon completion of his Ph.D. degree in 2016, he worked as a Research Associate with the Department of Earth Sciences, Centre for Polar Observation and Modelling, University College London, and the Jet Propulsion Laboratory, California Institute of Technology, Pasadena, CA, USA, between 2017 and 2020.

Henriette Skourup (Member, IEEE) received the M.Sc. degree in geophysics and the Ph.D. degree in satellite remote sensing of Arctic sea ice freeboard heights, gravity anomalies and dynamic topography from the University of Copenhagen, Copenhagen, Denmark, in 2004 and 2010, respectively.

She has more than 20 years of experience in the scientific and operational sea ice community. She has worked as a part-time Sea Ice Analyst with Operational Sea Ice Mapping Division, Danish Meteorological Institute, Copenhagen, from 1997 to 2004. Since 2004, she has been working with the Geodesy and Earth Observation Department, National Space Institute (DTU Space), Technical University of Denmark, Kongens Lyngby, Denmark, as a Research Scientist. Her research interests are sea ice thickness obtained from satellite altimetry. As a large part of her work includes validation of satellite altimetry missions, she has coordinated and participated in numerous airborne field campaigns in the Arctic.

René Forsberg is currently a Professor with DTU Space, Kongens Lyngby, Denmark, and leading the European Space Agency Climate Change Initiative for Greenland. He has worked extensively with geodetic, satellite and airborne research for cryosphere monitoring, general geodesy, and earth observation. He has taken the initiatives to, planned and led numerous field expeditions in Greenland, Svalbard, Arctic Canada, Arctic Ocean, Antarctica, as well as many regions of Asia and Africa, both as part of basic geodetic mapping, and airborne surveys for satellite validation. He is the Danish Chairman for the Scientific Commission on Antarctic Research and a member of the ESA Advisory Board for Earth Observation (ACEO).